

Master Thesis

Classification of Electron-Neutrino Events Based on
Final States Using New T2K Near Detectors
(T2K実験新型前置検出器を用いた
電子ニュートリノ反応の終状態に基づく分類)

January 26, 2024

Department of Physics, Graduate School of Science
The University of Tokyo
東京大学大学院理学系研究科物理学専攻

Hokuto Kobayashi
小林 北斗

Abstract

The T2K(Tokai-to-Kamioka) experiment is a long baseline neutrino oscillation experiment in Japan. T2K aims to observe the CP violation in the lepton sector. Until now, T2K has excluded the CP conservation with more than a 90% confidence level. In the T2K oscillation analysis, the uncertainty on the electron neutrino(ν_e) cross-section is one of the largest systematic uncertainties.

Each component of the T2K experiment has been upgraded in order to achieve better sensitivity. One of the major upgrades is a new detector in the near detector system (ND280).

In this thesis, the selection of ν_e interaction candidate events and their classification based on the final states using the upgraded ND280 are discussed. Better understanding and possible reduction of background events are possible by investigating each final state separately. Also, measurement of cross-sections in specific final states may be possible in the future. The ν_e charged current interactions without charged pions are selected with the efficiency and purity of 17.1% and 60.5%, respectively. The efficiency and purity for events with a charged pion are 9.3% and 38.0%, respectively. Based on the results of this study, possible improvements are discussed.

Contents

1	Introduction	4
1.1	Neutrino oscillation	4
1.1.1	Neutrino mixing matrix	4
1.1.2	Theory of neutrino oscillation	5
1.1.3	CP violation	6
1.2	Neutrino interaction	6
1.2.1	Neutrino interaction models	6
1.2.2	Nuclear effects	9
1.2.3	Electron neutrino interaction	9
2	T2K experiment	10
2.1	Overview	10
2.2	J-PARC accelerator and neutrino beamline	11
2.2.1	The J-PARC accelerator	11
2.2.2	The neutrino beamline	11
2.2.3	Off-axis method	13
2.3	Near detectors	14
2.4	Far detector: Super-Kamiokande(SK)	16
2.5	T2K recent results	17
2.5.1	Oscillation analysis results and systematic uncertainties	17
2.5.2	Electron neutrino cross-section measurements	19
2.6	T2K II	20
3	ND280 upgrade	22
3.1	Limitation of current ND280 performances	22
3.2	Detectors of upgraded ND280	22
3.2.1	SuperFGD	23
3.2.2	HA-TPC	24
3.2.3	TOF	24
3.3	Expected performances of the upgraded ND280	25
3.4	Status of ND280 upgrade	27
3.4.1	Assembly of SuperFGD	27
3.4.2	Commissioning of SuperFGD	27
3.4.3	Upgrade detectors	27
3.5	Subjects of this thesis	29

4	Monte Carlo simulation and reconstruction	30
4.1	Monte Carlo simulation	30
4.1.1	Simulation of neutrino beam and interaction sample	30
4.1.2	Particle gun sample	30
4.1.3	Detector response simulation	31
4.2	Reconstruction algorithms	32
4.2.1	Event reconstruction on SuperFGD	32
4.2.2	HA-TPC and TOF detector	33
4.2.3	Event reconstruction on other detectors	33
4.3	Particle identification by sub-detectors	34
4.3.1	SuperFGD PID	34
4.3.2	TPC PID	35
4.3.3	ECal PID	36
4.4	Proton and pion identification	36
5	Selection of ν_e-CC events	38
5.1	Vertex selection	39
5.2	Electron track indentification	40
5.2.1	Cone construction	41
5.2.2	EM shower identification	41
5.2.3	TPC and ECal PID	44
5.2.4	Electron/gamma separation	44
5.3	Other Particle identifications	46
5.4	Rejection of particles from outside of the fiducial volume	47
5.5	Selection result	47
5.5.1	Selected ν_e -CC events	49
5.5.2	Selected backgrounds events	49
6	Classification of ν_e-CC events	51
6.1	Classification based on final states	51
6.2	Study of background reduction for ν_e -CC inclusive event selection	52
6.2.1	γ background	53
6.2.2	$\bar{\nu}_e$ background	53
6.2.3	ν_μ background	55
6.3	Study of the exclusive final state selection for cross-section measurement	55
6.3.1	The CC0 π^\pm sample	55
6.3.2	The CC1 π^\pm sample	56
6.3.3	The selected CCmulti π^\pm events	56
7	Discussion	57
7.1	Impacts on T2K oscillation analysis	57
7.2	Future improvements	57
8	Summary	59

Chapter 1

Introduction

Neutrino is one of the elementary particles in the standard model with spin 1/2. It has three different flavors: electron neutrino, muon neutrino, and tau neutrino. Theories of neutrino mixing, neutrino oscillation, and neutrino interaction are described in this chapter.

1.1 Neutrino oscillation

1.1.1 Neutrino mixing matrix

Neutrino has flavor and mass eigenstates. The neutrino flavor eigenstates ν_α ($\alpha = e, \mu, \tau$) are described by the mass eigenstates ν_k ($k = 1, 2, 3$) and a lepton mixing matrix U known as Pontecorvo-Maki-Nakagawa-Sakata (PMNS) matrix,

$$\begin{pmatrix} \nu_e \\ \nu_\mu \\ \nu_\tau \end{pmatrix} = U \begin{pmatrix} \nu_1 \\ \nu_2 \\ \nu_3 \end{pmatrix} = \begin{pmatrix} U_{e1} & U_{e2} & U_{e3} \\ U_{\mu1} & U_{\mu2} & U_{\mu3} \\ U_{\tau1} & U_{\tau2} & U_{\tau3} \end{pmatrix} \begin{pmatrix} \nu_1 \\ \nu_2 \\ \nu_3 \end{pmatrix}. \quad (1.1)$$

The PMNS unitary matrix satisfies,

$$\sum_k U_{\alpha k}^* U_{\beta k} = \delta_{\alpha\beta} \quad \text{and} \quad \sum_\alpha U_{\alpha k}^* U_{\alpha j} = \delta_{kj} \quad (1.2)$$
$$(\alpha, \beta = e, \mu, \tau)(k, j = 1, 2, 3).$$

The mixing matrix has four physical parameters, three mixing angles ($\theta_{12}, \theta_{13}, \theta_{23}$) and one CP violating phase δ_{CP} . A parameterization of the Dirac neutrino mixing matrix is

$$U = \begin{pmatrix} 1 & 0 & 0 \\ 0 & c_{23} & s_{23} \\ 0 & -s_{23} & c_{23} \end{pmatrix} \begin{pmatrix} c_{13} & 0 & s_{13}e^{-i\delta_{CP}} \\ 0 & 1 & 0 \\ -s_{13}e^{-i\delta_{CP}} & 0 & c_{13} \end{pmatrix} \begin{pmatrix} c_{12} & s_{12} & 0 \\ -s_{12} & c_{12} & 0 \\ 0 & 0 & 1 \end{pmatrix} \quad (1.3)$$

$$= \begin{pmatrix} c_{12}c_{13} & s_{12}c_{13} & s_{13}e^{-i\delta_{CP}} \\ -s_{12}c_{23} - c_{12}s_{13}s_{23}e^{i\delta_{CP}} & c_{12}c_{23} - s_{12}s_{13}s_{23}e^{i\delta_{CP}} & c_{13}s_{23} \\ s_{12}s_{23} - c_{12}s_{13}c_{23}e^{i\delta_{CP}} & -c_{12}s_{23} - s_{12}s_{13}c_{23}e^{i\delta_{CP}} & c_{13}c_{23} \end{pmatrix} \quad (1.4)$$

where $c_{kj} \equiv \cos \theta_{kj}$ and $s_{kj} \equiv \sin \theta_{kj}$. The three mixing angles take values in the range of $0 \leq \theta_{kj} \leq \pi/2$ and the CP violating phase takes a value in the range of $-\pi \leq \delta_{CP} \leq \pi$.

1.1.2 Theory of neutrino oscillation

Neutrino oscillations are described as a consequence of a neutrino mixing of flavor states. A neutrino with flavor α is represented by a linear combination of flavor eigenstates,

$$|\nu_\alpha\rangle = \sum_k U_{\alpha k}^* |\nu_k\rangle \quad (\alpha = e, \mu, \tau). \quad (1.5)$$

The neutrino mass states $|\nu_k\rangle$ ($k = 1, 2, 3$) are the eigenstates of the Hamiltonian with energy eigenvalues E_k ,

$$\mathcal{H} |\nu_k\rangle = E_k |\nu_k\rangle, \quad (1.6)$$

$$E_k = \sqrt{p^2 + m_k^2}, \quad (1.7)$$

where p is a neutrino momentum and m_k is a mass eigenstate value. The time evolution of neutrino is expressed by the Schrodinger equation,

$$i \frac{d}{dt} |\nu_k(t)\rangle = \mathcal{H} |\nu_k(t)\rangle. \quad (1.8)$$

The propagation in vacuum is expressed as

$$|\nu_k(t)\rangle = e^{-iE_k t} |\nu_k\rangle. \quad (1.9)$$

Evolutions of flavor eigenstates in vacuum are expressed as

$$|\nu_\alpha(t)\rangle = \sum_k U_{\alpha k}^* e^{-iE_k t} |\nu_k\rangle \quad (1.10)$$

$$= \sum_k \sum_\beta U_{\alpha k}^* U_{k\beta} e^{-iE_k t} |\nu_\beta\rangle. \quad (1.11)$$

The neutrino oscillation probability from ν_α to ν_β in vacuum is calculated as

$$P(\nu_\alpha \rightarrow \nu_\beta) = |\langle \nu_\beta | \nu_\alpha(t) \rangle|^2. \quad (1.12)$$

For an ultrarelativistic neutrino, energy eigenvalues can be approximated as $E_k \simeq E + \frac{m_k^2}{2E}$, where $E = |\mathbf{p}|$ is the neutrino energy and $t \simeq L$ where L is a flight distance. As a consequence, the oscillation probability is expressed as

$$\begin{aligned} P(\nu_\alpha \rightarrow \nu_\beta) &= \delta_{\alpha\beta} - 4 \sum_{k<j} \text{Re} [U_{\alpha k} U_{\alpha j}^* U_{\beta k}^* U_{\beta j}] \sin^2 \left(\frac{\Delta m_{kj}^2 L}{4E} \right) \\ &\quad \pm 2 \sum_{k<j} \text{Im} [U_{\alpha k} U_{\alpha j}^* U_{\beta k}^* U_{\beta j}] \sin \left(\frac{\Delta m_{kj}^2 L}{2E} \right) \end{aligned} \quad (1.13)$$

with the difference of the mass squared $\Delta m_{kj}^2 = m_k^2 - m_j^2$, where \pm means neutrino(+) and anti-neutrino(-) cases.

In the case of ($\alpha = \beta$), the survival probability is expressed as

$$P(\nu_\alpha \rightarrow \nu_\alpha) = P(\bar{\nu}_\alpha \rightarrow \bar{\nu}_\alpha) = 1 - 4 \sum_{k < j} |U_{\alpha k} U_{\alpha j}^*|^2 \sin^2 \left(\frac{\Delta m_{kj}^2 L^2}{4E} \right) \quad (1.14)$$

which is the same for both neutrinos and anti-neutrinos.

1.1.3 CP violation

The charge-conjugation and parity-reversal (CP) symmetry of fundamental particles is a symmetry between matter and antimatter. CP violation does not appear in the survival channel since the survival probability is the same for both neutrinos and anti-neutrinos. Thus, CP violation is only measurable in the oscillation channel with the comparison between $P(\nu_\alpha \rightarrow \nu_\beta)$ and $P(\bar{\nu}_\alpha \rightarrow \bar{\nu}_\beta)$ in the case of $\alpha \neq \beta$. The difference in the oscillation probability is

$$\Delta P_{\alpha \rightarrow \beta} \equiv P(\nu_\alpha \rightarrow \nu_\beta) - P(\bar{\nu}_\alpha \rightarrow \bar{\nu}_\beta) \quad (1.15)$$

$$= 4 \sum_{k < j} \text{Im} [U_{\alpha k} U_{\alpha j}^* U_{\beta k}^* U_{\beta j}] \sin \left(\frac{\Delta m_{kj}^2 L}{2E} \right). \quad (1.16)$$

As all present accelerator neutrino beamlines are dedicated to producing a muon neutrino beam, the CP violation can be measured in neutrino oscillations via $\nu_\mu \rightarrow \nu_e$ appearance using accelerator neutrinos. The difference between $P(\nu_\mu \rightarrow \nu_e)$ and $P(\bar{\nu}_\mu \rightarrow \bar{\nu}_e)$ is calculated as

$$\Delta P_{\mu \rightarrow e} = -16J \sin \left(\frac{\Delta m_{32}^2 L}{4E} \right) \sin \left(\frac{\Delta m_{21}^2 L}{4E} \right) \sin \left(\frac{\Delta m_{31}^2 L}{4E} \right) \quad (1.17)$$

where $J \equiv \text{Im} [U_{\mu 1}^* U_{e 1} U_{\mu 2} U_{e 2}^*]$ is known as Jarlskog invariant given by

$$J \equiv \frac{1}{8} \cos \theta_{13} \sin 2\theta_{12} \sin 2\theta_{23} \sin 2\theta_{13} \sin \delta_{CP}. \quad (1.18)$$

Conditions for CP violation in neutrino oscillations are

$$\theta_{kj} \neq 0, \quad m_k \neq m_j, \quad \text{and} \quad \delta_{CP} \neq 0, \pi. \quad (1.19)$$

1.2 Neutrino interaction

1.2.1 Neutrino interaction models

Present neutrino experiments measure neutrino interaction with nuclear targets. Since neutrinos are electrically neutral, they do not interact electromagnetically. As neutrinos do not undergo strong interaction, they can only interact via weak interactions: charged current(CC) and neutral current(NC) interactions.

Figure 1.1 shows cross-sections of neutrino-nucleus charged current interactions in the sub-GeV energy range.

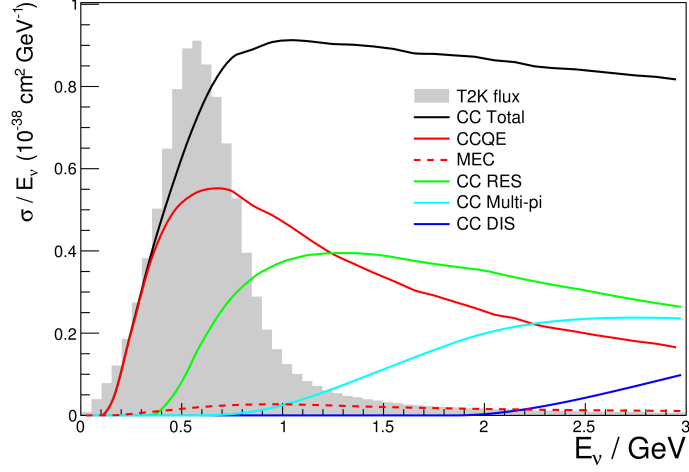


Figure 1.1. Muon-neutrino cross sections of neutrino-nucleus interactions in ^{12}C . The shaded area is the expected neutrino beam flux in T2K.[1]

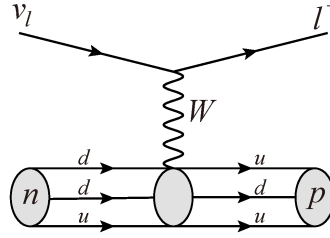


Figure 1.2. A diagram of CCQE.[2]

Charged current quasi-elastic scattering(CCQE)

CC quasi-elastic scattering is the two-body process between a neutrino and a nucleus. This is the dominant mode in the sub-GeV energy range. Figure 1.2 shows the diagram of CCQE. It produces a charged lepton and a nucleus in the final state,

$$\nu_l + n \rightarrow l^- + p, \quad (1.20)$$

$$\bar{\nu}_l + p \rightarrow l^+ + n. \quad (1.21)$$

Charged current resonance scattering(CCRes)

CC resonance scattering is the dominant mode in a few GeV energy ranges. In the resonance scattering process, a nucleon struck by a neutrino can become a baryon resonant state decaying into a final state with a nucleon and a pion, kaon, η or γ . For example, CCRes single-pion production is

$$\nu_l + N \rightarrow N^* + l^- \rightarrow N' + l^- + \pi^+ \quad (1.22)$$

where N, N' are a nucleon and N^* is the resonant state. Figure 1.3 shows this diagram.

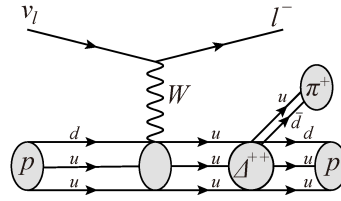


Figure 1.3. A diagram of CCRes single pion production.[2]

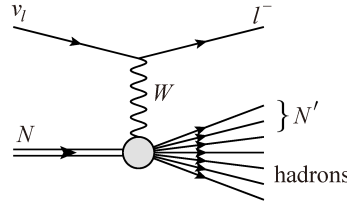


Figure 1.4. A diagram of CCDIS.[2]

Charged current deep inelastic scattering(CCDIS)

In the neutrino energy range over about 3 GeV, the dominant interaction mode is CC deep inelastic scattering. In this energy range, neutrinos can interact directly with quarks inside a nucleon. It breaks the nucleon and produces a jet of hadrons as shown in Figure 1.4 and written by

$$\nu_l + N \rightarrow l^- + N' + \text{hadrons.} \quad (1.23)$$

Charged current coherent pion production(CCcoh)

In a coherent pion production process, a neutrino interacts with the whole nucleus and produces a pion without changing the quantum state of the nucleus shown in Figure 1.5.

$$\nu_l + N \rightarrow l^- + N' + \pi^+. \quad (1.24)$$

It is not a dominant process which corresponds to a few percent of a CCQE process.

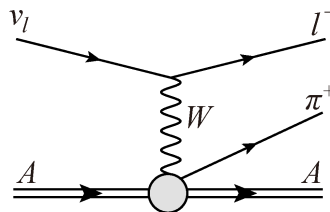


Figure 1.5. A diagram of CCcoh.[2]

Experiment	CC inclusive	CCQE-like (π less)	π production	Target
ArgoNeuT	[8]	-	-	Ar
COHERENT	[9]	-	-	I
MicroBooNE	[10], [11]	[12]	-	Ar
MINER ν A	-	[13]	-	CH
NO ν A	[14]	-	-	CH ₂
T2K	[5], [6], [7]	-	-	CH, H ₂ O

Table 1.1. Published measurements of electron neutrino and antineutrino cross sections from modern accelerator-based neutrino experiments.[15]

1.2.2 Nuclear effects

In Section 1.2.1, the interaction between neutrinos and nucleons is considered. In addition, because nucleons are bound inside a nucleus, various effects due to the nucleus (nuclear effects) need to be taken into account.

The initial momentum of the nucleon inside a nucleus can affect the neutrino interactions. The target nucleon is not free but bound in the nucleus. Then it is necessary to take into account the multi-nucleon interaction to include scattering off a bound state, such as the 2-particle 2-hole process(2p2h) and n-particle n-hole(npnh)[3][4].

The final state particles such as pions, protons, and neutrons at neutrino interactions can re-interact with the nuclear medium. These interactions are called final-state interactions. Such particles can be absorbed and get their kinematics distorted or eject additional hadrons.

1.2.3 Electron neutrino interaction

Since all present accelerator neutrino beamlines are dedicated to producing a muon neutrino beam, muon neutrino cross-sections have been measured with high statistics, and the electron neutrino cross-section has been measured with small statistics and large uncertainty. Measurements of ν_e -CC interaction cross sections at a few GeV regions have been performed by some experiments as shown in Table 1.1. Also, the electron neutrino cross-section of π production has not been measured with an accelerator neutrino beam.

In T2K, the cross section was measured in 2014[5], 2015[6] and 2020[7]. The result in 2020 will be shown in Chapter 2.

Chapter 2

T2K experiment

2.1 Overview

The T2K(Tokai to Kamioka) experiment is a long baseline neutrino oscillation experiment in Japan. T2K has acquired neutrino beam data since January 2010.

It measures ν_μ to ν_e oscillation and ν_μ disappearance using ν_μ beam generated at the Japan Proton Accelerator Research Complex(J-PARC). Neutrinos are detected at the near detector(ND280) located at 280 m from the beam target and the far detector Super-Kamiokande located 295 km from the target as shown in Figure 2.1.

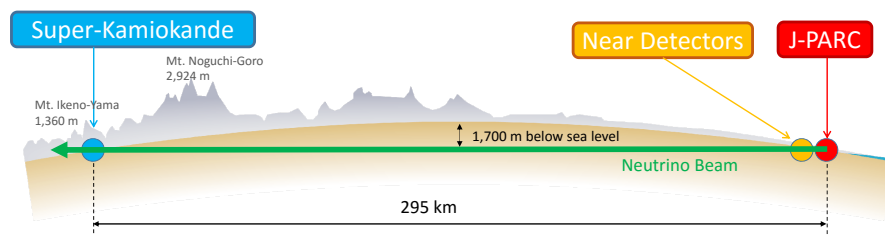


Figure 2.1. A T2K overview.[16]

2.2 J-PARC accelerator and neutrino beamline

2.2.1 The J-PARC accelerator

The J-PARC accelerator consists of three accelerators as shown in Figure 2.2: a 400 MeV linear accelerator(LINAC), a 3 GeV rapid cycling synchrotron(RCS), and a 30 GeV main ring(MR) synchrotron. Protons are accelerated to 30 GeV by MR and extracted to the neutrino beamline. A proton spill consists of eight bunches separated at intervals of 580 ns. It is produced every 1.36 s with a power of 760 kW at the last physics run in December 2023.

2.2.2 The neutrino beamline

Neutrino beamline is composed of two sections: the primary beamline and the secondary beamline. In the primary beamline, the extracted proton beam is transported to the production target of the secondary beamline. The secondary beamline consists of a target station, a decay volume, and a beam dump as shown in Figure 2.3. Protons strike a graphite target and generate secondary pions and other hadrons. Secondary pions are focused by three magnetic horns and decay into muons and muon neutrinos in the decay volume.

The two beam modes can be switched by controlling the polarity of the horn. Each mode is forward horn current(FHC) or reverse horn current(RHC) with producing beams in neutrino or anti-neutrino enhanced mode, respectively. The dominant decay channels of a pion are

$$\pi^+ \rightarrow \mu^+ + \nu_\mu, \quad (2.1)$$

$$\pi^- \rightarrow \mu^- + \bar{\nu}_\mu. \quad (2.2)$$

In the neutrino energy region above 3 GeV, dominant contributions are from kaon decay such as:

$$K^+ \rightarrow \mu^+ + \nu_\mu, \quad (2.3)$$

$$K^+ \rightarrow \pi^0 + \mu^+ + \nu_\mu, \quad (2.4)$$

$$K^- \rightarrow \mu^- + \nu_\mu, \quad (2.5)$$

$$K^- \rightarrow \pi^0 + \mu^- + \bar{\nu}_\mu. \quad (2.6)$$

Also, a neutrino beam contains electron neutrinos via the following decay channels,

$$K^+ \rightarrow \pi^0 + e^+ + \nu_e, \quad (2.7)$$

$$\mu^+ \rightarrow e^+ + \nu_e + \bar{\nu}_\mu, \quad (2.8)$$

$$K^- \rightarrow \pi^0 + e^- + \bar{\nu}_e, \quad (2.9)$$

$$\mu^- \rightarrow e^- + \bar{\nu}_e + \nu_\mu. \quad (2.10)$$

Figure 2.4 shows the predicted flux as a function of neutrino energy at the near detector in FHC. Electron neutrinos comprise only about 1% of the T2K neutrino beam. Hadrons are stopped by the beam dump located 109m from the target. High-energy muons can penetrate the beam dump and can be detected by the muon monitor(MUMON) used for monitoring a neutrino beam.

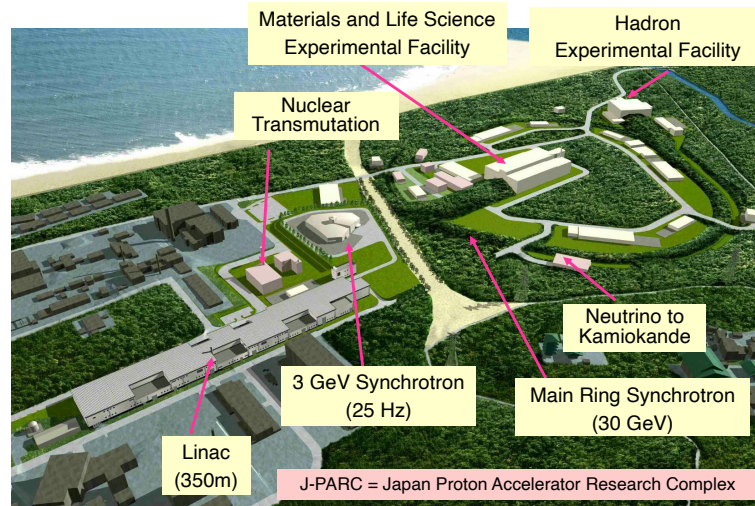


Figure 2.2. Overview of J-PARC accelerators.[17]

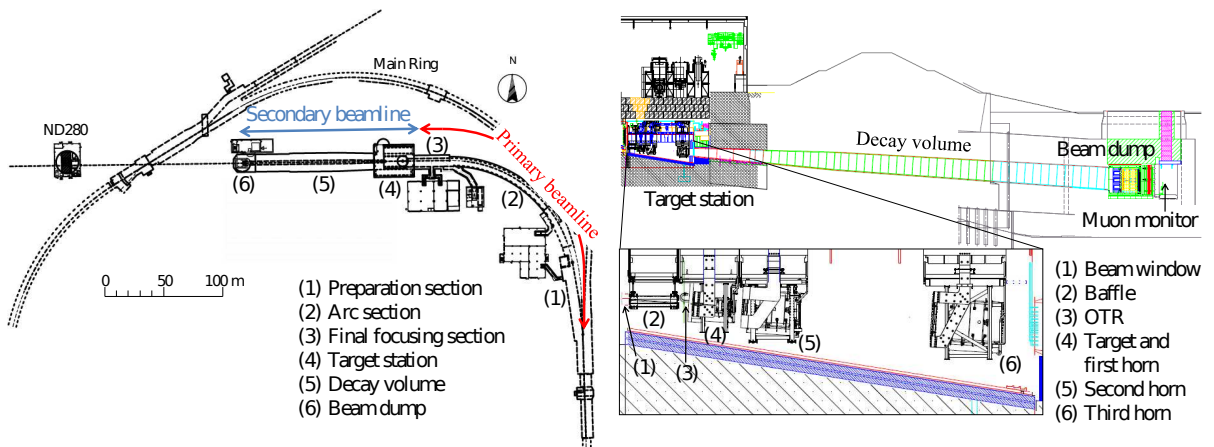


Figure 2.3. Left: overview of neutrino beamline. Right: side view of the secondary beamline.[18]

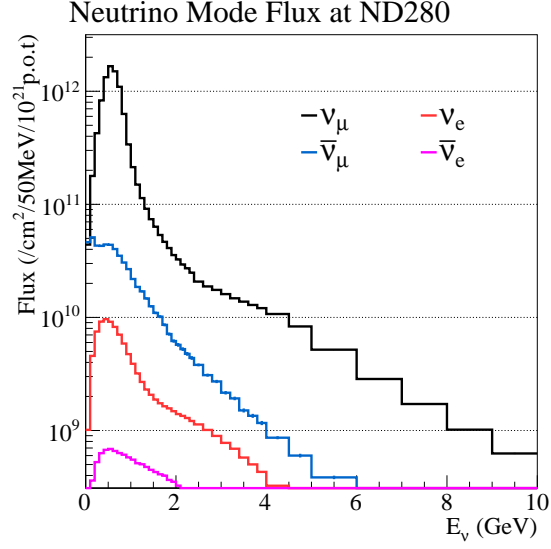


Figure 2.4. The predicted flux as a function of neutrino energy at ND280 in FHC mode.[7]

2.2.3 Off-axis method

T2K adopts the off-axis method to generate the narrow-band neutrino beam. The neutrino beam is directed at an angle with respect to the far detector direction. The off-axis angle is set at 2.5° , and the muon neutrino beam is generated to have peak energy at about 0.6 GeV.

Figure 2.5 shows the neutrino oscillation probability and the simulated neutrino flux with on-axis(0°) and off-axis angles. The off-axis angle of 2.5° maximizes the oscillation probability at Super-Kamiokande.

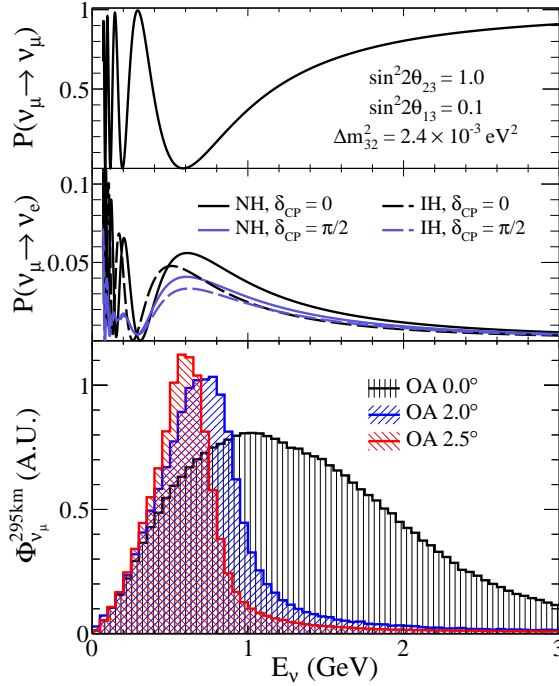


Figure 2.5. The neutrino oscillation probability and muon neutrino flux in T2K neutrino beam.[19]

2.3 Near detectors

To constrain the uncertainties on the neutrino interaction models and neutrino beam flux of the neutrino oscillation analysis, T2K has the near detector complex so-called ND280 at the off-axis angle of 2.5° and 280 m downstream from the target. A schematic view of ND280 is shown in Figure 2.6. ND280 consists of several sub-detectors and the UA1 magnet which provides a 0.2 T magnetic field.

Each sub-detector is introduced in the following.

Fine grained detector(FGD)

Two FGDs provide target mass for neutrino interaction and track charged particles. They are sandwiched by three TPCs. They have some scintillator sub-modules, each sub-module consists of an x-layer and a y-layer which each has 192 scintillator bars as shown in Figure 2.7. Each scintillator bar has the size of $184 \text{ cm} \times 0.96 \text{ cm} \times 0.96 \text{ cm}$. Scintillator bars are aligned in either x or y direction perpendicular to the beam direction. The upstream FGD called FGD1 has 15 sub-modules and the downstream FGD called FGD2 consists of 7 sub-modules and 6 water sub-modules filled with water.[20]

Time projection chamber(TPC)

Three TPCs are for tracking charged particles generated from neutrino interactions in FGDs. It is filled with the gas that is a mixture of $\text{Ar} : \text{CF}_4 : i\text{C}_4\text{H}_{10}$ (95% : 3% : 2%)[22].

The TPCs can reconstruct tracks in three dimensions and measure the charge and momentum for charged particles with the magnetic field. It allows also particle identification

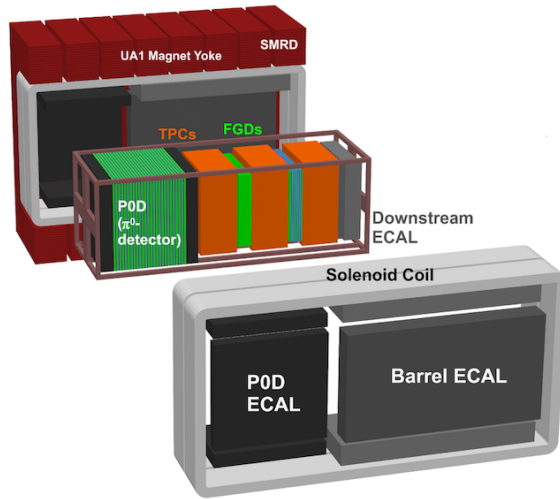


Figure 2.6. Overview of ND280.[18]

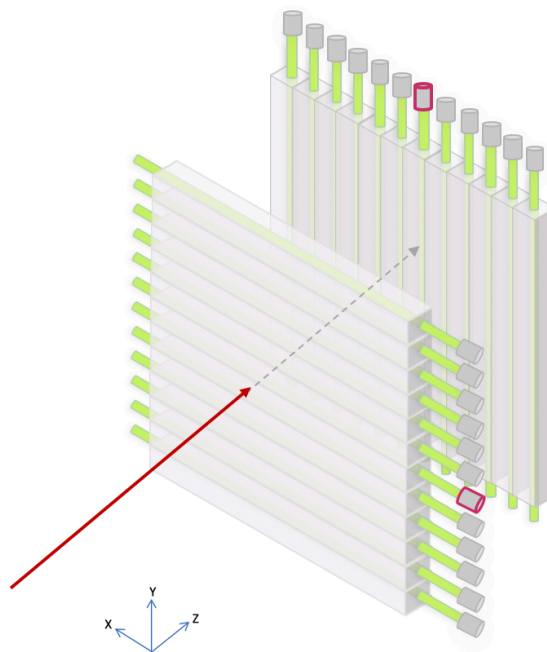


Figure 2.7. A structure of FGD sub-module.[21]

by measuring the energy loss and the momentum.

Pi zero detector(P0D)

P0D is designed to measure neutral current π^0 production. The central module of the detector consists of scintillator bars, water bags, and sheets of lead and brass. P0D is replaced with upgrade detectors described in Chapter 3.

Electromagnetic calorimeter(ECal)

The ECal is a sampling electromagnetic calorimeter surrounding the inner detectors(P0D, FGDs, TPCs). It has layers of plastic scintillator bars with lead absorber sheets[18]. There are 13 independent ECal modules in ND280: P0D ECal with 6 modules that surrounds P0D, Barrel ECal with 6 modules that surrounds FGDs and TPCs, and 1 Downstream ECal.

2.4 Far detector: Super-Kamiokande(SK)

Figure 2.8 shows a schematic view of Super-Kamiokande which is the far detector of the T2K to detect neutrinos after traveling 295 km. It is a cylindrical water Cherenkov detector filled with 50 kton of water. The detector is separated into two volumes: the inner detector and the outer detector. The inner wall of the inner detector is covered by 11200 20-inch photomultiplier tubes (PMTs) and the outer wall is covered by 1185 8-inch PMTs. They detect Cherenkov light of charged particles generated from neutrino interactions. The outer detector is used for external background rejection. Events of Cherenkov rings with a muon-like and an electron-like are shown in Figure 2.9.

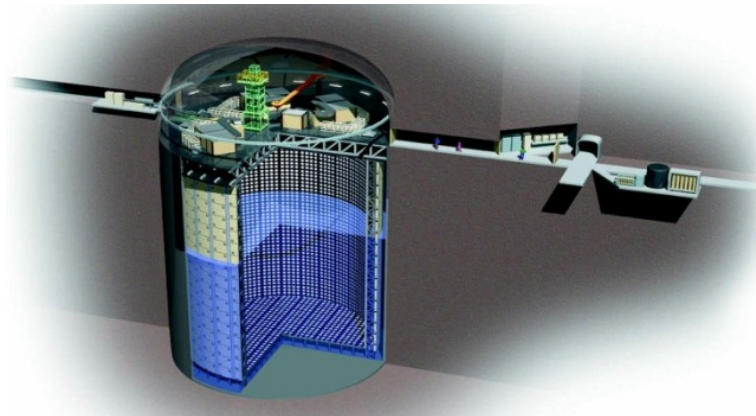


Figure 2.8. A schematic view of Super-Kamiokande.[23]

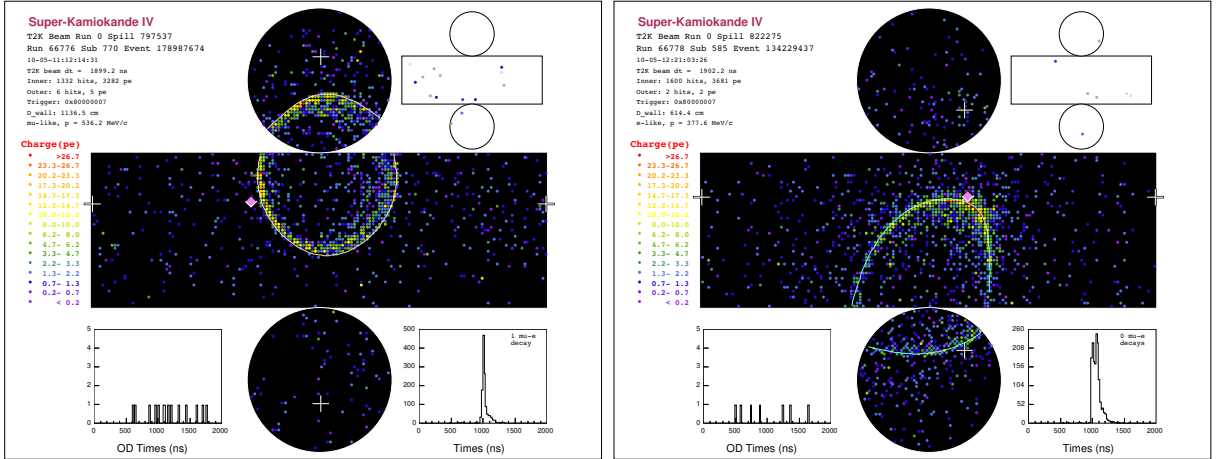


Figure 2.9. Event displays of Cherenkov rings. Left: muon-like, right: electron-like.[18]

2.5 T2K recent results

2.5.1 Oscillation analysis results and systematic uncertainties

The main goal of the T2K experiment is to search for CP violation in lepton by measuring the neutrino oscillation. T2K has published the latest results using the data collected from 2010 to 2020[24]. The data-set corresponds to 1.97×10^{21} protons on target(POT) in the FHC mode and 1.63×10^{21} POT in the RHC mode.

Figure 2.10 shows the $\Delta\chi^2$ distribution in δ_{CP} and the confidence intervals. The result indicates the CP conserving values $\delta_{CP} = 0, \pi$ are excluded at 90% confidence level.

The predicted neutrino event rate in the far detector is calculated by,

$$N_{\nu_\mu}(E_\nu) = P(\nu_\mu \rightarrow \nu_\mu)\sigma(E_\nu)\varphi(E_\nu)\varepsilon(E_\nu) \quad (2.11)$$

$$N_{\nu_e}(E_\nu) = P(\nu_\mu \rightarrow \nu_e)\sigma(E_\nu)\varphi(E_\nu)\varepsilon(E_\nu) \quad (2.12)$$

where $\sigma(E_\nu)$ is neutrino cross-section in water, $\varphi(E_\nu)$ is beam flux, and $\varepsilon(E_\nu)$ is the detection efficiency. Systematic uncertainty of the predicted relative number of ν_e and $\bar{\nu}_e$ is shown in Table 2.1.

Neutrino event sample in Super-Kamiokande

SK events are comprised of five independent samples. For both neutrino and anti-neutrino beam modes, there is a sample of events that contain a single muon-like ring(1μ) and only a single electron-like ring with no decay electron from pions($1e0de$). These single lepton samples are dominated by CCQE interactions. In the neutrino beam mode there is a sample containing an electron-like ring as well as the signature of an additional delayed electron from the decay of a charged pion and subsequent muon($1e1de$)[25]. Table 2.2 shows the expected and observed number of events with FHC: 1.96×10^{21} POT and RHC: 1.63×10^{21} POT.

Compared to other samples, the $1e1de$ sample has an excess in the observed number of events compared to the expectation. In particular, it is noticeable in the low energy range of electrons under 200 MeV/c as shown in Figure 2.11. Similar excess is also reported

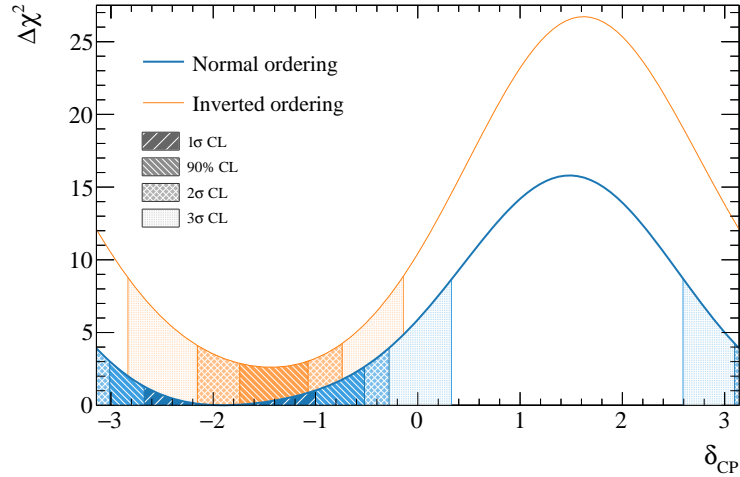


Figure 2.10. The $\Delta\chi^2$ distribution in δ_{CP} from fitting to the data with reactor constraint applied. The shaded confidence intervals are calculated using the Feldman-Cousins method.[24]

Type of Uncertainty	$\nu_e/\bar{\nu}_e$ Candidate Relative Uncertainty (%)
Super-K Detector Model	1.5
Pion Final State Interaction and Rescattering	1.6
Neutrino Production and Interaction Model Constrained by ND280 data	2.7
ν_e and $\bar{\nu}_e$ Interaction Model	3.0
Nucleon Removal Energy in Interaction Model	3.7
Modeling of Neutral Current Interactions with Single γ Production	1.5
Modeling of Other Neutral Current Interactions	0.2
Total Systematic Uncertainty	6.0

Table 2.1. The systematic uncertainty on predicted relative number of ν_e and $\bar{\nu}_e$ candidates in the Super-Kamiokande with no decay electrons.[25]

Beam mode	SK sample	Expected rate	Observed
FHC	1μ	378.693	318
FHC	$1e$	102.543	94
RHC	1μ	144.749	137
RHC	$1e$	17.330	16
FHC	$1e1de$	10.024	14

Table 2.2. Expected and observed number of neutrino-events at SK

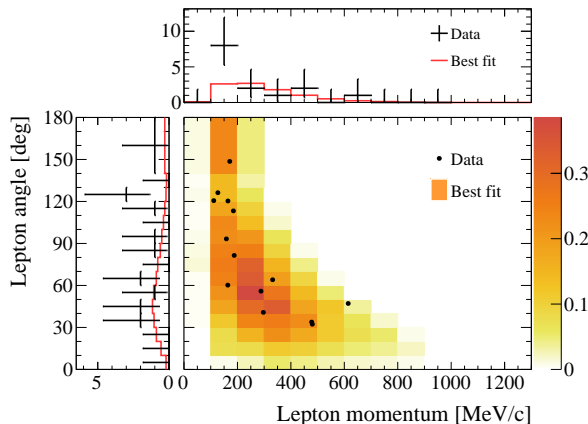


Figure 2.11. The events for the $1e1de$ SK samples, shown in reconstructed electron momentum and the angle between the neutrino beam and the lepton in the lab frame. The insets show the events projected onto each single dimension, and the red line is the expected number of events.[24]

from the joint analysis [26] with the SK atmospheric neutrinos sample which has higher statistics than T2K beam neutrinos. One possible reason for this excess is due to the neutrino-nucleus interaction model. To investigate this in more detail, it will be useful to measure electron-neutrino interactions with samples classified by their final states.

2.5.2 Electron neutrino cross-section measurements

To search for CP violation, the oscillated ν_e and $\bar{\nu}_e$ are measured at Super-Kamiokande. The uncertainty of ν_μ interaction models has been constrained by the measurement with the near detector since ν_μ is the main component of the neutrino beam at the near detector. The ν_e cross-section is estimated using the neutrino-nucleus interaction models. One of the dominant uncertainties in the δ_{CP} measurement at T2K is due to ν_e and $\bar{\nu}_e$ cross-section models. Thus, it is important to measure directly the ν_e cross-sections at the near detector for the uncertainty reduction.

Measurements of ν_e -CC interaction cross-sections at a few GeV regions have been performed by some experiments. In T2K, the cross-section was measured in 2014[5], 2015[6], and 2020[7]. For the T2K result in 2020, the $\nu_e(\bar{\nu}_e)$ cross-sections are measured with ND280 using FHC mode: 11.92×10^{20} POT and RHC mode: 6.29×10^{20} POT data. The reconstructed momentum distributions of selected $\nu_e(\bar{\nu}_e)$ are shown in Figure 2.12. This analysis selected 697 ν_e candidate events in total for FHC mode.

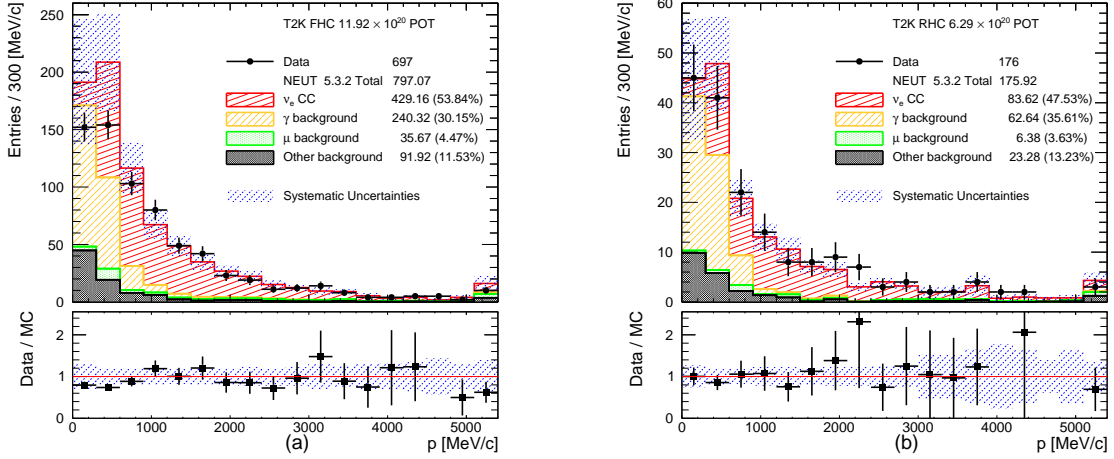


Figure 2.12. The reconstructed momentum distributions of ν_e -CC candidates for FHC mode(Left) and RHC mode(Right).[7]

There are large amounts of gamma background coming from neutrino interactions. In particular, the gamma background remains in the low momentum region which gives large systematic uncertainties since the cross-section of ν_μ - γ production has large systematic uncertainties. The purity and efficiency of ν_e were estimated to be 26 % and 54 %, respectively, with simulation. The ν_e cross-section is measured to be

$$\sigma_{\nu_e} = 6.62 \pm 1.32(stat) \pm 1.30(syst) / 10^{-39} \text{ cm}^2/\text{nucleon}. \quad (2.13)$$

Statistical and systematic uncertainties are larger than systematic errors of predicted ν_e cross-section. Therefore, it is necessary to achieve the selection with more statistics and less background to reduce both of the uncertainties.

2.6 T2K II

T2K II is the second phase of the experiment to search for CP violation with more than 3σ significance level. To achieve the goal, we will collect the data of 1.0×10^{22} POT by 2027 when the Hyper-Kamiokande experiment starts. Toward increasing the neutrino data, the J-PARC MR and the neutrino beamline will be upgraded. As statistics increase, the effects of the systematic uncertainties will be more crucial to the δ_{CP} measurement. Thus, the ND280 and the Super-Kamiokande are upgraded.

Beam upgrade

The J-PARC MR were upgraded shortening the time of the beam cycle from 2.48 s to 1.36 s in 2023, and achieved a power of 760 kW at the last physics run in December 2023. The MR upgrade aims to shorten the time of the beam cycle from 1.36 s to 1.16 s and to increase the beam power up to 1.3 MW in the future. To focus secondary pions, the power supply of the horn was increased from 250 kA to 320 kA. Also cooling systems for the horn and the graphite target were upgraded.

SK-Gd

Before 2020, the Super-Kamiokande had been operated with pure water. Gadolinium(Gd) was loaded into the water to increase the detection efficiency of neutrons. Neutrons are captured by Gd and excited Gd nuclei emit photons which have a total energy of 8 MeV. In 2020 Gd was loaded with a mass concentration of 0.01 % to the Super-Kamiokande, and the capture efficiency is about 50 %. In 2022 Gd was loaded with a mass concentration of 0.03 %, and the capture efficiency is 75 %.

ND280 upgrade

Since this study is performed with the upgraded near detector, the ND280 upgrade is described in detail in [Chapter 3](#).

Chapter 3

ND280 upgrade

3.1 Limitation of current ND280 performances

To constrain the uncertainties on the neutrino interaction models of the neutrino oscillation analysis, T2K measures neutrino interactions on ND280: FGDs, TPCs, and ECals.

However, those detectors have acceptance only around beam direction due to the detector configurations. Since TPCs are located in the front and back of each FGD to detect particles going through the beam direction, the ND280 has a lower efficiency to detect particles scattering to large angles.

In addition, ND280 has a weakness in detecting low-momentum particles. Each submodule of FGD is composed of two orthogonal layers aligned in the vertical and horizontal directions. It requires three hits in each direction to reconstruct a track. The shortest reconstructable track length is about 6 cm, which corresponds to about 600 MeV/c in the case of a proton track. Moreover, ND280 has a low sensitivity in detecting low-momentum electrons. To select electron neutrino interactions, the conversion of gamma decayed from π^0 is the large background and makes uncertainty described in Chapter 2.5.2.

3.2 Detectors of upgraded ND280

To reduce the systematic uncertainties with neutrino measurement in those limited spaces inside the UA1 magnet, T2K is in the process of ND280 upgrade to replace P0D with SuperFGD, two high-angle TPCs(HA-TPC) which sandwich SuperFGD from above and below, and the Time of flight detector(TOF) surrounding SuperFGD and HA-TPC as shown in Figure 3.1.

SuperFGD consists of 1 cm cube of plastic scintillators to give a 4π acceptance by detecting light from a cube. It allows short-track detection and is expected to have high and uniform tracking efficiency. There are capabilities to separate electrons from gamma conversion. HA-TPCs are expected to detect particles scattered at a large angle coming from SuperFGD.

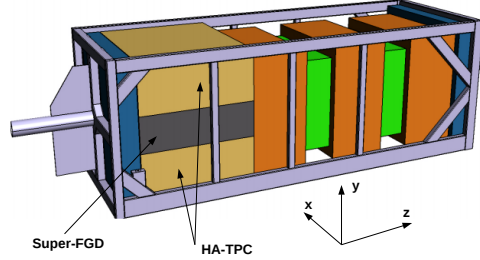


Figure 3.1. A schematic view of the upgraded ND280 and coordinate axis.[27]

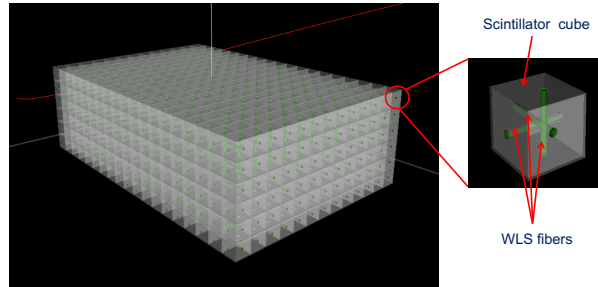


Figure 3.2. A schematic view of the SuperFGD.[27]

3.2.1 SuperFGD

SuperFGD consists of $192 \times 182 \times 56$ plastic scintillators which are 10.27 mm cubes. Charged particles can be detected within the fiducial volume (FV) which is the space of scintillator cubes stacked. SuperFGD has a FV of $(x : 1.97) \times (z : 1.87) \times (y : 0.575) \text{ m}^3$ which is twice as large as FGD1 FV.

Each cube has three holes to pass through the wavelength shifting(WLS) fibers. Scintillation lights are transported in WLS fibers and detected by multi-pixel-photon-counters(MPPC) on one side. A schematic view of the SuperFGD is shown in Figure 3.2.

Scintillator cube

The scintillator cubes are made by UNIPLAST Co. (Vladimir, Russia). They are mainly made of polystyrene doped with 1.5% of paraterphenyl(PTP) and 0.01% of POPOP. They are covered with a reflecting layer which is produced with a chemical etching of the scintillator surface. The layer has the thickness within 50 to 80 μm . Each cube has three orthogonal through holes with a diameter of 1.5 mm.

WLS fiber

WLS fibers are used to collect and transport light from scintillators. Y-11(200) is a WLS fiber produced by KURARAY Co.[28], also used in the ND280. It has a multi-cladding structure with a 1.0 mm diameter.

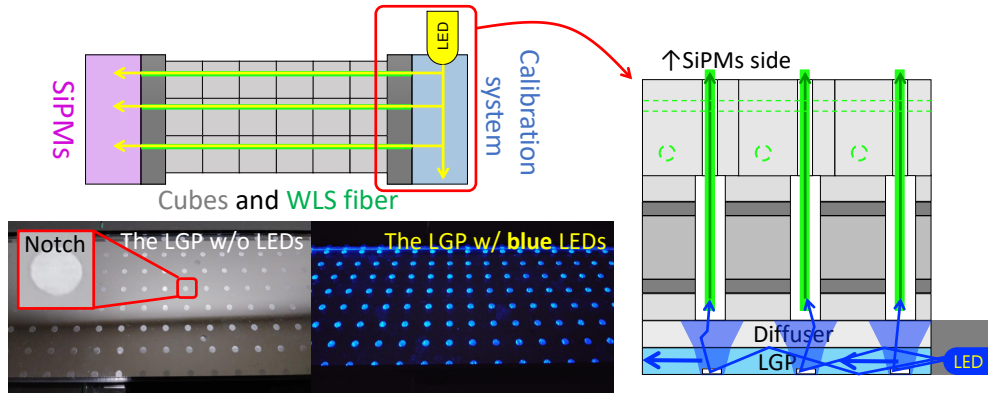


Figure 3.3. The conceptual drawing of the light injection method for a large number of channels and a picture of the LGP prototype.[31]

MPPC

The MPPCs which are produced by Hamamatsu Photonics K.K., are single photon avalanche diode(SiPM) devices to detect the lights from WLS fibers. MPPC type S13360-1325PE[29] is equipped on SuperFGD. It has advantages over that of ND280, such as a lower dark noise rate, crosstalk probability between pixels, and afterpulse probability. A set of 64(8×8) MPPCs are mounted on a single PCB(MPPC-PCB) and the PCB is attached to SuperFGD.

Electronics

The Cherenkov imaging telescope integrated read out chip(CITIROC)[30] is a front-end ASIC developed by Omega laboratory at Ecole Polytechnique. It can readout 32 channel of SiPM outputs at the same time.

LED calibration system

To measure and check signal gain and pedestal, the LED calibration system is attached on the opposite side of MPPC[31]. LED lights are transported by two sub-modules: the light-guide-plate(LGP) and the diffuser. LGP scatters the lights as shown in Figure 3.3. The diffuser allows lights to be inserted into WLS fibers uniformly.

3.2.2 HA-TPC

Two HA-TPCs have a size of $2.0 \times 0.8 \times 1.8$ m and are similar to TPCs described in Section 2.3. It consists of a gas-tight rectangular box sub-divided by a common high-voltage electronic cathode located in the middle and supporting the eight micromegas readout modules as shown in Figure 3.4.

3.2.3 TOF

Six TOF detectors surrounding SuperFGD and HA-TPC are shown in Figure 3.5. Each module consists of scintillator bars and the light is detected by MPPCs on both sides of

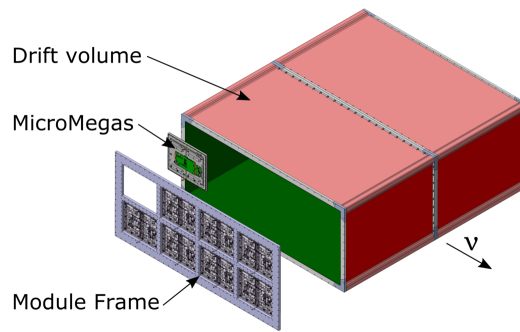


Figure 3.4. A schematic view of the HA-TPC.[27]

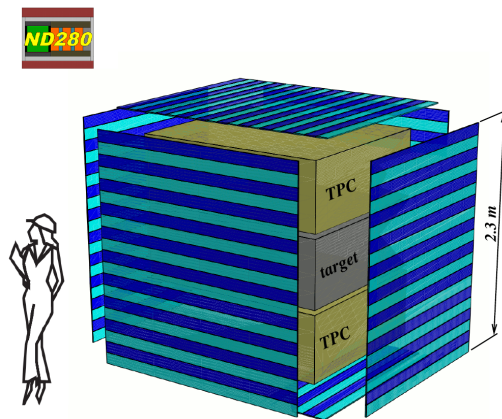


Figure 3.5. A layout of the TOF.[27]

the bars.

3.3 Expected performances of the upgraded ND280

Figure 3.6 shows muon tracking efficiency with the original and upgraded ND280. Super-FGD and HA-TPCs are expected to have the capability to track particles scattered at large angles from the beam direction.

Also, there are capabilities to reconstruct low-momentum protons and pions with efficiencies of about 90% as shown in Figure 3.7.

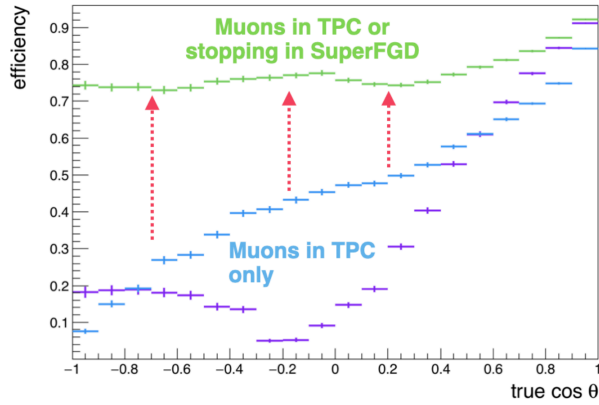


Figure 3.6. The muon tracking efficiency as a function of the cosine of the angle with respect to the z axis (θ). The purple line is the original ND280 configuration. The blue line is the upgraded configuration with muons in TPC only, also the green line includes the muons stopping SuperFGD.[32]

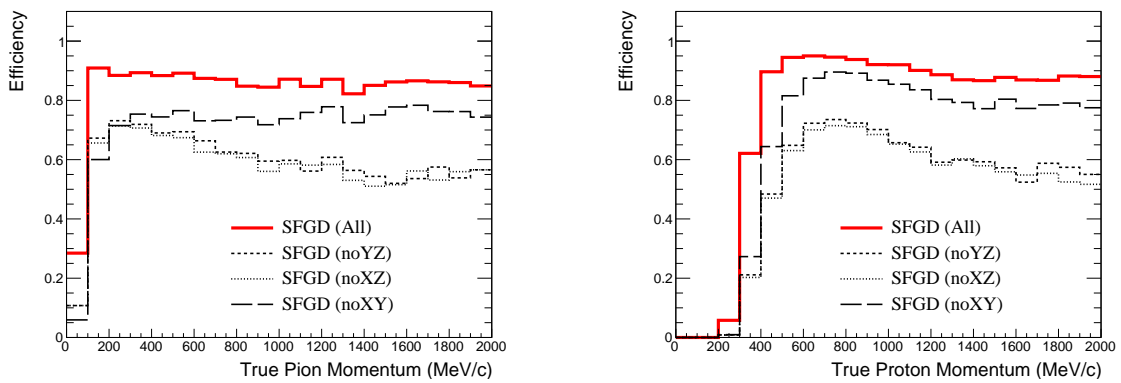


Figure 3.7. Expected track reconstruction efficiencies for pions(left) and protons(right) in SuperFGD with three readout views or with only two readout views.[27]

3.4 Status of ND280 upgrade

3.4.1 Assembly of SuperFGD

SuperFGD was assembled in J-PARC from October 2022 to April 2023. Figure 3.8 shows the construction progress described in the following.

- Making a SuperFGD box to put the cubes, and stacking cubes(October to December). Cubes are stacked one layer at a time vertically aligning each layer. The layer consists of 192×182 cubes held by fishing lines.
- Inserting WLS fibers and attaching MPPC(January to February). A total of 55888 fibers were passed through the box hole into the cube, one by one. After fiber insertion, MPPC-PCBs were attached to the surface. We implemented and used a database system that can register the attached position and a serial number of MPPC-PCB with a network device. Figure 3.9 shows the situation of MPPC attachment using the database system.
- Attaching LED calibration module and light shielding by dark sheets(March).
- Attaching cables to MPPCs, and testing of light shielding and cable connectivity(April).

3.4.2 Commissioning of SuperFGD

Towards neutrino beam data taking, the response of SuperFGD was tested with front-end electronics from April 2023 to December 2023. Commissioning aims to check detector response and calibrate detector settings which were done using the LED calibration system and taking cosmic muon data. Also, network settings and cable connections were done at the same time.

From April to September, those responses were checked on the ground before installing into ND280-pit underground. In October, SuperFGD was installed into the ND280-pit and checked in the pit until December.

In December 2023, T2K took neutrino beam data. SuperFGD was operated with about 3/4 of the readout channels because not all the front-end electronics were ready for installation. The data taking was considered as a part of technical commissioning and useful to establish the operation of the new detector. The full operation is expected in spring 2024 after the installation of the remaining electronics.

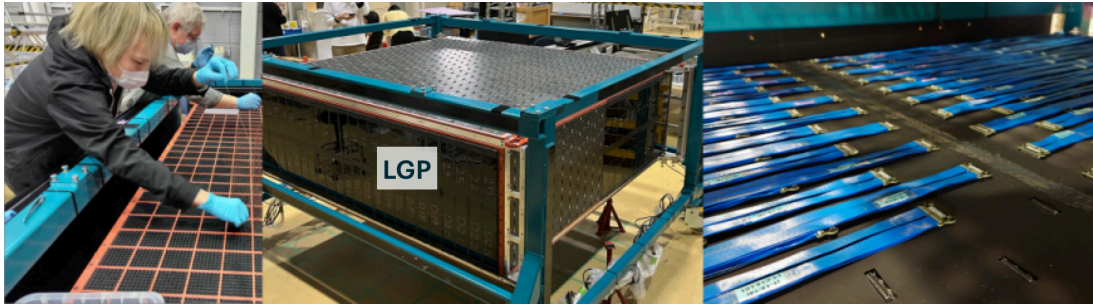
3.4.3 Upgrade detectors

The bottom HA-TPC was installed in ND280, and the top HA-TPC is planned to be installed in spring 2024. TOFs were installed except for those to the left and right of the beam. The left and right ones will be installed in spring 2024.

In December 2023, neutrino beam data were taken with these upgrade detectors and original ND280 detectors. The full upgrade is scheduled to be completed and beam data will be acquired in the spring 2024.



(a) Left: Cube layer stacking, middle: The cube layer stacking finished, right: After closing box



(b) Left: WLS fiber insertion, middle: LGPs were attached, right: cables were attached.

Figure 3.8. The situations of SuperFGD construction

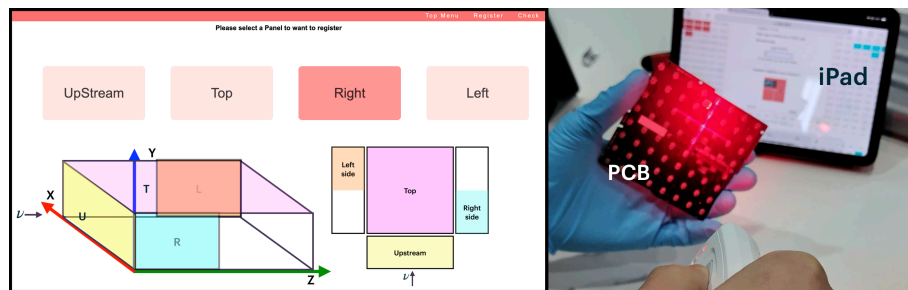


Figure 3.9. A display of the database system(Left) and the situation to register MPPC to the database system with iPad[33](Right).

3.5 Subjects of this thesis

The uncertainty of electron neutrino cross-section is one of the systematic sources of the predicted number of ν_e interactions in Super-Kamiokande for δ_{CP} measurements. Electron neutrino cross-section measurement with current ND280 has large uncertainties due to a significant gamma background contamination.

Algorithms for electron reconstruction and ν_e -CC event selection using the upgraded ND280 have been developed in the past [17]. It assumed the true vertex position because the vertex finding algorithm for the ν_e events was not ready.

In this thesis, we attempt to further understand the background by classifying the electron neutrino candidate events based on their final states using the upgraded ND280. A new vertex finding algorithm has been established to provide a more realistic estimate of performance.

Such classification may also lead to the measurement of cross-sections in specific final states. Since the electron neutrino $CC1\pi$ cross-section measurement has not been measured with all present accelerator neutrino beamlines, understanding neutrino cross-sections in exclusive final states helps to investigate the possible systematics in oscillation analysis, e.g., the excess electron neutrino $CC1\pi$ event in SK.

Chapter 4

Monte Carlo simulation and reconstruction

4.1 Monte Carlo simulation

The analysis in this thesis uses two types of samples: a neutrino interaction sample and a particle gun sample, generated by a Monte Carlo simulation(MC).

4.1.1 Simulation of neutrino beam and interaction sample

A neutrino interaction sample is generated by a neutrino beam simulation and a neutrino interaction simulation. In the T2K ND280 analysis, the MC simulation begins with generating neutrino flux. The proton-nucleus interactions inside the graphite target and the decay and interaction of generated particles in the secondary beamline are simulated. The hadron production cross-section is tuned based on the external measurements.

The neutrino beam flux is the input for NEUT 5.6.0[34] to simulate neutrino interactions on the materials of ND280 and the magnet. This study uses a neutrino interaction MC sample with 9.89225×10^{20} POT of FHC mode. The number of simulated neutrino events for each of the $\nu_\mu(\bar{\nu}_\mu)$ -CC, $\nu_e(\bar{\nu}_e)$ -CC, and NC interactions are shown in Table 4.1. They are separately shown for events inside and outside the SuperFGD fiducial volume(FV).

The number of simulated ν_e -CC events classified by the number of charged pions and protons leaving the target nucleus is shown in Table 4.2. Protons are required to have energies above 200 MeV, while no energy threshold is applied to pions.

4.1.2 Particle gun sample

Particle gun samples are generated to study the behavior of each particle in the detector. They are also used for the training of multivariate analysis such as particle identification. The five types of particle gun samples were generated with different particles: e^\pm , μ^\pm , π^\pm , p and γ . Each event contains a single primary particle starting inside the SuperFGD FV. Particle gun samples are generated with the weighted momentum distribution based on

Interaction	Inside FV	Out of FV
ν_μ -CC	144633	2442605
$\bar{\nu}_\mu$ -CC	4568	82297
ν_e -CC	2701	57357
$\bar{\nu}_e$ -CC	240	5095
NC	47927	645612
Total	200069	3232966

Table 4.1. Number of simulated neutrino interaction events.

Final state	CC0 π^\pm 0 p	CC0 π^\pm 1 p	CC0 π^\pm multi- p	
Events	18	1025	492	
	CC1 π^\pm 0 p	CC1 π^\pm 1 p	CC1 π^\pm multi- p	CCmulti π^\pm
	240	480	116	330

Table 4.2. Number of events for ν_e -CC interaction types categorized by the number of pions and protons in the final state. The multi- p requires two or more protons, the multi- π^\pm requires a total of two or more π^\pm and π^- .

the neutrino interaction on ND280 and the magnet of the MC sample. The characteristics of the particle gun samples are summarized in Table 4.3.

4.1.3 Detector response simulation

The passage of particles through the detector material is simulated based on a Geant4[35]. Figure 4.1 shows the geometry of ND280 detectors as well as the magnet which is implemented using the Geant4 package.

The response of the SuperFGD detector is simulated following the flow as shown in Figure 4.2. As a first step, the number of generated photons is calculated based on the hit timing and energy deposits in the scintillator cubes. In this step, the light leakage into adjacent cubes, which is called crosstalk, is simulated. The response of the scintillator cube is tuned based on the results of the beam test[36].

The second step simulates light transport by the WLS fiber. In this step, the number of photons at the MPPC is calculated taking into account the attenuation of light in the fiber and the reflection of light at the opposite end of the fiber to the MPPC.

As a third step, signals from the MPPC are simulated. In each MPPC channel, photons are converted to pixel hits. Dark noise, inter-pixel crosstalk, and afterpulses are simulated for each pixel.

In the last step, the response of the front-end electronics is simulated, and the timing

Particle	e^\pm	μ^\pm	π^\pm	p	γ
Momentum	[0, 3.5 GeV]	[0, 2.5 GeV]	[0, 1.5 GeV]	[0, 1.5 GeV]	[0, 1.5 GeV]
Angle	Isotropic in 4π				
Position	Uniform in the fiducial volume of SuperFGD				

Table 4.3. The characteristics of the particle gun samples

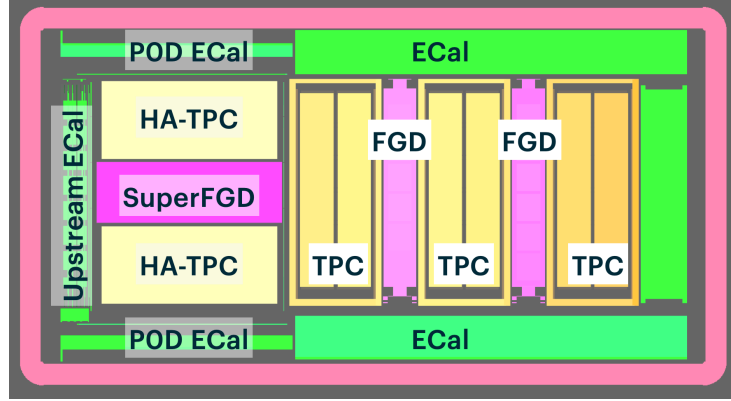


Figure 4.1. Input detector geometries for Geant4 simulation(side view).

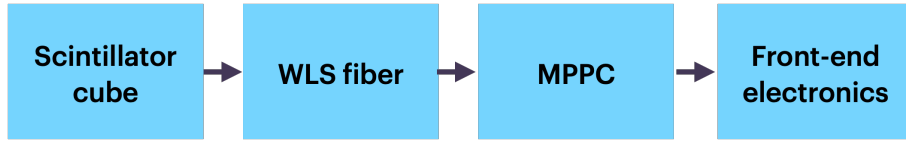


Figure 4.2. The flow of detector response simulation for SuperFGD.

and charge information from each channel are stored.

4.2 Reconstruction algorithms

Each sub-detector reconstruction is applied to the neutrino interaction samples. The reconstructed hits and tracks of each sub-detector are grouped and matched by the timing and distance of each reconstructed object.

4.2.1 Event reconstruction on SuperFGD

A brief overview of SuperFGD reconstruction is given here, and the detail is described in [17]. The flow of reconstruction algorithms for SuperFGD is shown in Figure 4.3. To separate hits from different interactions in a spill, MPPC hits are divided into groups separated by time gaps. If there is a gap of more than 100 ns between hits, the hits are divided into separate clusters.

Two-dimensional MPPC hits in three directions are converted into three-dimensional cube hits by considering every possible combination of fiber cross points as hits. The charge is assigned to each cube based on the event topology to minimize χ^2 of charge hit given by

$$\chi^2(\{q_c\}) = \sum_f \frac{[Q_f - \mathcal{Q}_f(\{q_c\})]^2}{Q_f} \quad (4.1)$$

where q_c is the light generated in the cube, Q_f is the charge measured on the fiber f and $\mathcal{Q}_f(\{q_c\})$ is the expected charge for fiber f as a function of the set of light yields in the cubes. The hit timing is calculated with an average of the three two-dimensional MPPC hit timing within 2.5 ns.



Figure 4.3. The flow of reconstruction algorithms for SuperFGD.

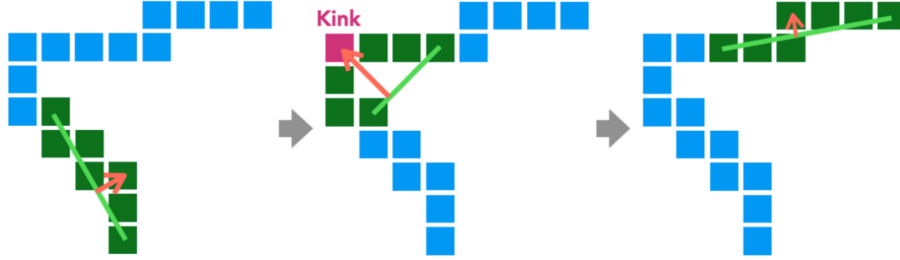


Figure 4.4. Kink finding method. The green squares are sub-sequence hits scanned. The orange line is the distance of the middle hit from the line between the two end hits.[17]

The three-dimensional hits are clustered by using the DBSCAN method[37]. Starting from an arbitrary hit, neighboring hits within a 1.6 cm radius are clustered. The clustering is repeated over connected hits until no more neighboring hits can be found. Then, starting from another unconnected hit, we repeat the same process for all the left hits. Also, each cluster is separated at the branching point found by Prim’s algorithm to make a minimum spanning tree(MST)[38].

Clusters are separated at a kink defined as the point where a cluster is bent. A kink is searched for to scan over every eight sub-sequence hits in a cluster. If the distance of the middle hit from the line between the two end hits is over 2.0 cm, the middle hit is defined to be a kink (see Figure 4.4). The kink and cluster edges can be candidates of neutrino interaction vertex.

A particle track is built as a result of fitting the clusters that have more than four hits. After track fitting, the cube hits are replaced with node objects of the time dependent with ordered in a certain direction. Also, this step can merge cross-talk to nodes. The not-fitted clusters are stored as cluster objects.

4.2.2 HA-TPC and TOF detector

HA-TPC and TOF detectors readout hits and detect particle tracks, but these reconstruction algorithms are not implemented yet at this time. Therefore in this study, tracks entering HA-TPC and TOF are not analyzed.

4.2.3 Event reconstruction on other detectors

For TPC reconstruction, two-dimensional hits are collected in a field cage and three-dimensional hits are reconstructed with the calculation of the drift speed of an ionized electron.

ECals readout 2D hits from two directions alternately and 3D hits are reconstructed.

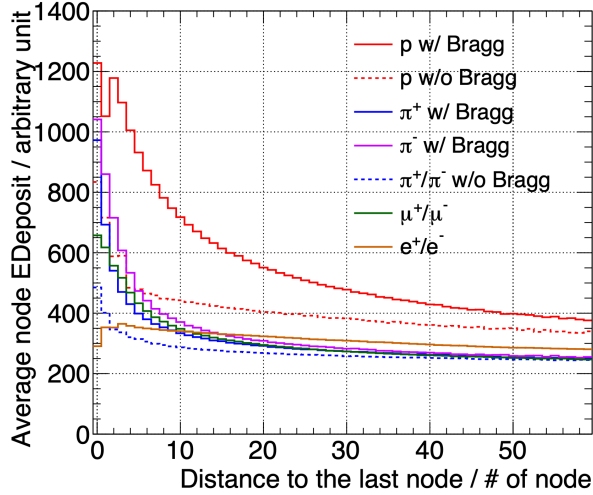


Figure 4.5. Node energy patterns of particle gun sample in SuperFGD. Only particles stopping in SuperFGD are considered. The "w/ Bragg" and "w/o Bragg" mean particles stopping with Bragg peak or without Bragg peak due to interacting with nucleons.[40]

Type of variable	variable description
Track length	-
Total track energy deposition	-
Node distance	Distance between each node and its nearest node
Node deposition	Energy deposition of each node
Node energy deposition fluctuation	-

Table 4.4. Input variables for GBDT to identify particles based on track in SuperFGD.

4.3 Particle identification by sub-detectors

Particle identification(PID) algorithms are applied to reconstructed tracks for identifying particle types: muons, pions, protons, and electrons. Since identifying electrons needs electromagnetic(EM) shower reconstruction, the reconstruction needs a dedicated algorithm that is important for this study and it is described in Chapter 5.

4.3.1 SuperFGD PID

When particles lose energy and finally stop in the detector, the energy deposit is increased significantly, which is also referred to as Bragg peak. Particles passing through the SuperFGD are identified by the reconstructed node energy pattern with Bragg peak as shown in Figure 4.5. The particle identification with the Gradient-Boosting Decision Tree(GBDT) method with TMVA[39] framework, developed for the selection of ν_μ events[40], is used. Using the input variables listed in Table 4.4, the probability that a particle is of each type is calculated. The results of the GBDT for each particle gun sample are shown in Figure 4.6. The particle type with the highest probability is selected.

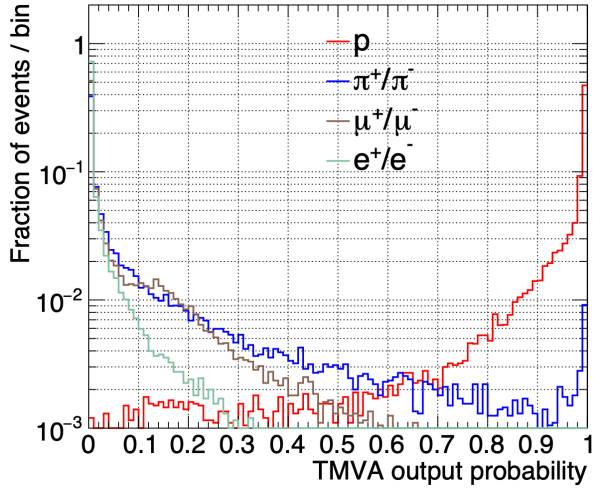


Figure 4.6. GBDT result of each particle based on track in SuperFGD.[40]

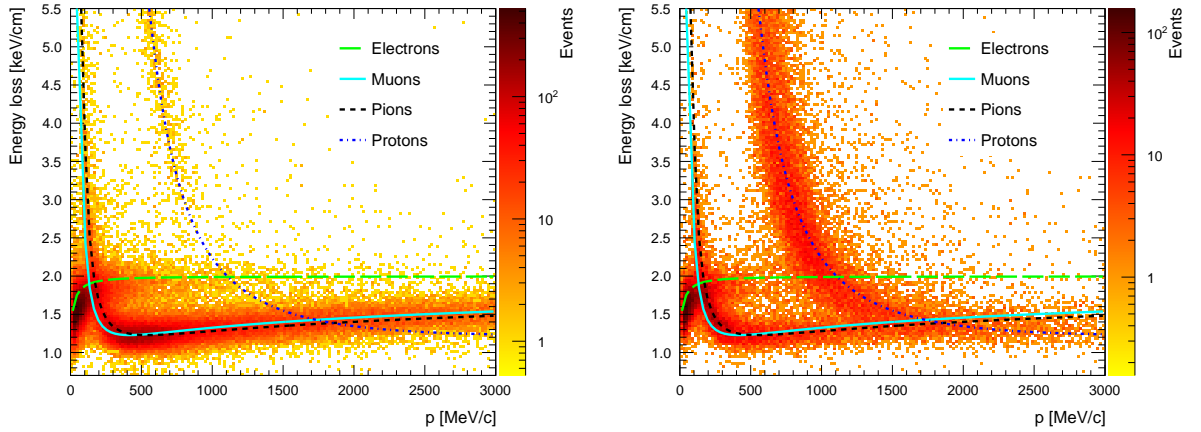


Figure 4.7. Energy loss in the TPC of tracks starting from FGD1 in real data. Left: negatively charged tracks. Right: positively charged tracks. Each curve shows the expected energy loss curves for electrons, muons, pions, and protons.[7]

4.3.2 TPC PID

The TPCs provide track reconstruction with a momentum resolution of about 8% for 1 GeV/c particles and measurement of energy loss per unit length with a resolution of $7.8 \pm 0.2\%$ for minimum ionizing particles. The measured energy loss per unit length and momentum are used to calculate the difference between the measured mean ionization and the expected one divided by the resolution. The standard deviation of the calculated value becomes the likelihood of each particle: proton, pion, muon, and electron[22]. Figure 4.7 shows the relationships between the energy loss and the momentum in TPC.

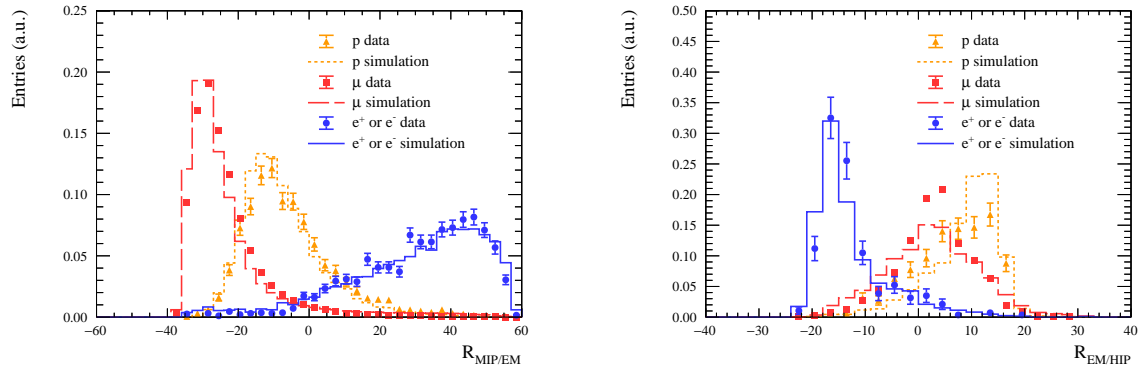


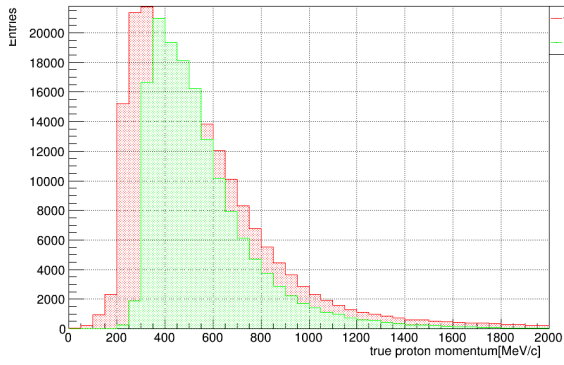
Figure 4.8. Performance of the ECal PID using samples of cosmic and through-going muons, electrons, positrons from gamma conversions, and protons from neutrino interactions. Left: Log-likelihood ratio of the ECal track-shower ($R_{MIP/EM}$) PID. Right: Log-likelihood ratio of the ECal electron-proton ($R_{EM/HIP}$) PID for showers with $R_{MIP/EM} > 0$ and the momentum larger than 600 MeV/c. Plots are normalized to unity.[7]

4.3.3 ECal PID

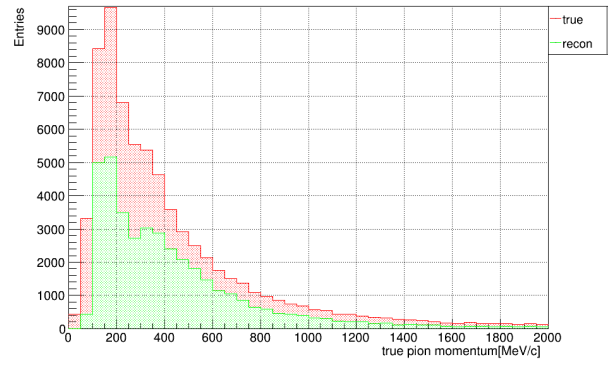
ECal PID can separate electrons from other particles such as muons, pions, and protons with the likelihood ratio which is calculated by comparing the TPC momentum with the ECal energy deposit based on each type of particle hypothesis: minimum ionization particle(MIP) track, EM-shower, and highly ionizing stopping particle(HIP) like a proton. The ECal PID performance is shown in Figure 4.8. In both cases, electrons are identified with a threshold of 0.

4.4 Proton and pion identification

For the particles stopping inside SuperFGD FV, protons and pions are identified only by SuperFGD PID. For the particles entering TPC after SuperFGD, they are identified if they are recognized by either PID. Applying these PIDs, protons are reconstructed over the 300 MeV/c region, pions are reconstructed over the 100 MeV/c region as shown in Figure 4.9.



(a) Proton



(b) Pion

Figure 4.9. Momentum distribution of MC true and reconstructed particles. Red histogram shows the momentum distribution of the MC true, green histogram shows the momentum distribution of the reconstructed particle whose type is correctly identified. This distribution does not include misidentified types of particles.

Chapter 5

Selection of ν_e -CC events

This chapter describes the selection of ν_e -CC events. The inclusive ν_e -CC sample, which includes all ν_e -CC events in SuperFGD, is selected. The classification into exclusive event samples is discussed in the next chapter.

The ν_e -CC inclusive selection flow is shown in Figure 5.1. First, the following two conditions (pre-selection) are applied.

- The relevant ND280 sub-detector has good data quality and beam spill. This step is not necessary for MC samples.
- Events have at least one reconstructed track in SuperFGD.

After the pre-selection step, the following algorithms are applied to each event.

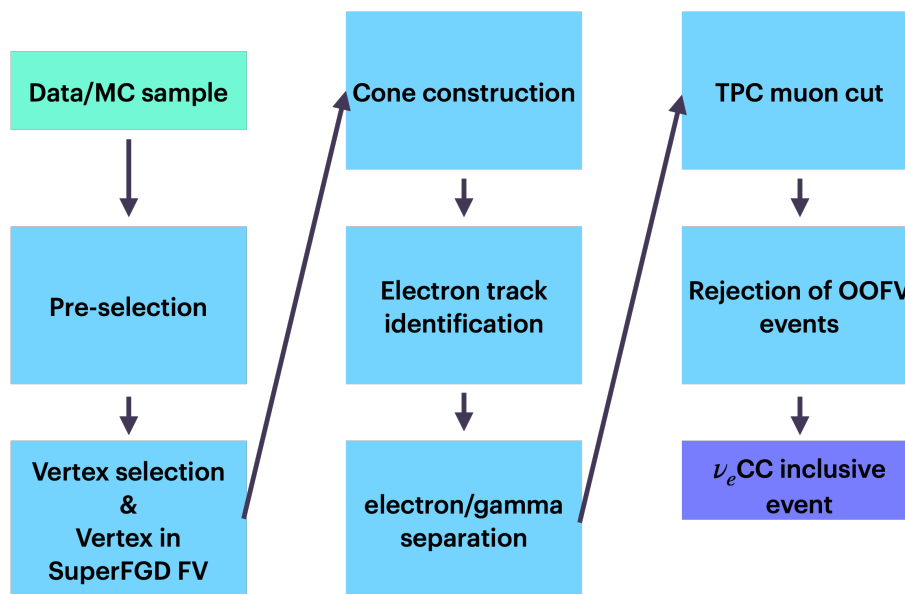


Figure 5.1. Algorithm flows of ν_e -CC inclusive selection.

5.1 Vertex selection

As neutrinos can interact anywhere in the sub-detectors, a neutrino interaction vertex has to be identified. A neutrino interaction vertex is identified as a muon starting point for the selection of muon neutrino events. A vertex cannot be selected from the lepton starting point for an electron neutrino event, since an EM-shower is generated by a high energy electron in the electron neutrino events.

The previous analysis uses the true vertex of MC. For realistic estimation of the selection performance, this analysis uses the reconstructed vertex selected from candidates reconstructed with the pattern recognition algorithm as described in Chapter 4. A neutrino interaction vertex is chosen from vertex candidates with track shape and proton-like track starting position. The vertex selection flow is as follows:

1. The following conditions are required as a pre-vertex selection to reject vertex located on intersection or EM-shower.
 - (i) A vertex candidate is not located at the middle point of any track.
 - (ii) For tracks longer than 30 cm, a vertex candidate is not at the endpoint based on the direction determined from time information.
 - (iii) The time of a vertex is not more than 2 nsec after the earliest timing of vertex candidates.
2. Vertex identification with two methods.
 - (a) Choose the vertex to which the longest track is connected. The longest track is assumed to be a lepton-track or a charged pion track.

	Detection ratio	30 mm-ratio
2-(a) only	94.7%	82.8%
Combined 2-(a) and 2-(b)	95.7%	85.6%

Table 5.1. The performance of the vertex selection in ν_e -CCQE mode by methods of only 2-(a), and combined 2-(a) and 2-(b). The detection ratio is the ratio of detecting vertex inside SuperFGD. The 30 mm-ratio is the ratio that a vertex is selected within 30 mm from the position of the MC true vertex.

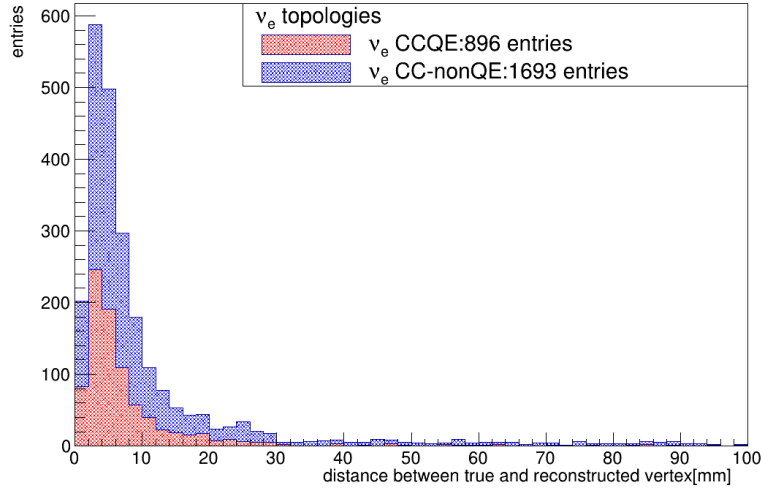


Figure 5.2. Distribution of the distance between true and selected vertex. The red area is ν_e -CCQE events and the blue area is not ν_e -CCQE events. The histograms are stacked.

- (b) Apply proton PID which is described in Section 4.3 to each track connected to vertex candidates. Then, choose the vertex connected to the starting point of a proton-like track.
3. Identify the vertex by comparing two vertices chosen in Step 2-(a) and 2-(b)
 - (a) In the case of a proton-like track escaping to other sub-detectors or having a length longer than 20 cm, the vertex is identified by Step 2-(b).
 - (b) If the vertex is not identified by Step 3-(a), the vertex is identified by Step 2-(a).

Finally, a vertex is required to be inside FV.

The method in Step 2-(a) was developed after the previous analysis[17]. Combining the method in Step 2-(b), the efficiency with which vertex of the ν_e -CC interaction inside FV is found, and the ratio that a vertex is selected within 30 mm from the position of the MC true vertex are increased as shown in Table 5.1. Figure 5.2 shows the distance between a selected vertex and the position of MC true vertex in ν_e -CC interaction.

5.2 Electron track identification

For the electron track reconstruction, EM-shower reconstruction and, TPC and ECal PID are applied to a reconstructed track. As EM-shower reconstruction and cone construc-



Figure 5.3. Algorithm flow for electron track detection.

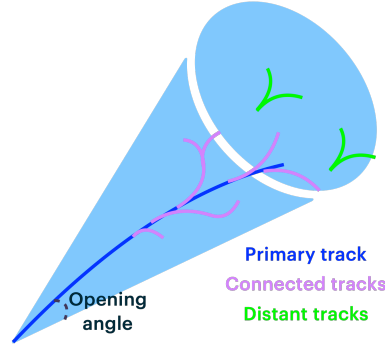


Figure 5.4. A schematic view of a cone object. Blue: primary track, purple: connected tracks, light green: distant tracks, and light blue: cone.

tion were developed in the previous study[17], this study uses in combination of the two algorithms with the algorithm flow as shown in Figure. 5.3.

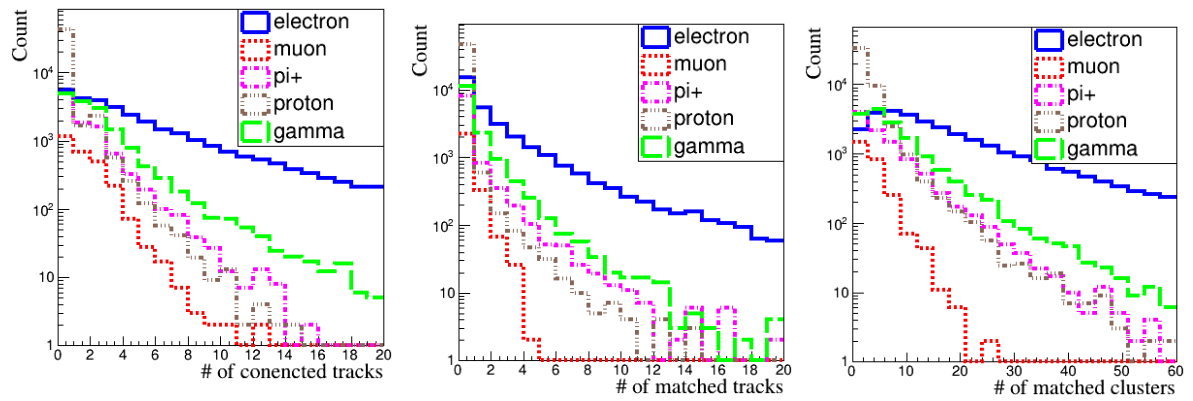
5.2.1 Cone construction

To reconstruct the EM-shower, the reconstructed tracks, and clusters are grouped in this step with the objects-shaped cone as shown in Figure 5.4.

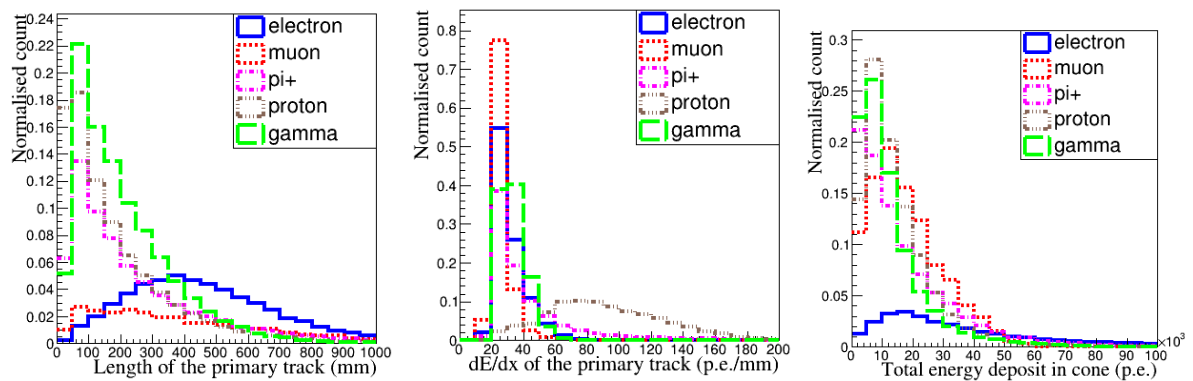
A cone object has three types of track: primary, connected, and distant track. Tracks connected to the vertex are the primary tracks. A connected track or cluster has a minimum distance between the primary or other connected tracks is less than 30 mm. Any tracks whose first node is located inside of 60° from the direction of the primary track are distant tracks. The EM-shower reconstruction is processed based on the cone object.

5.2.2 EM shower identification

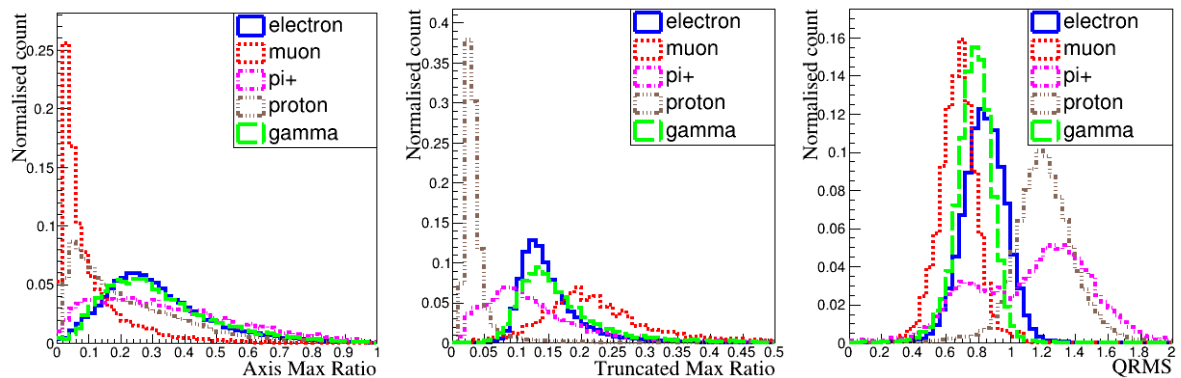
As SuperFGD has a 1.9 m length in beam direction, many electrons generate EM-shower flying in the volume. The shower reconstruction is necessary to identify an electron track and it is performed by the Gradient Boosted Decision Tree(GBDT) method[17]. GBDT input variables for EM-shower reconstruction are in Table 5.2 and each input value distribution of the particle gun sample is shown in Figure 5.5. GBDT training results of EM-shower versus protons, pions, and muons are shown in Figure 5.6.



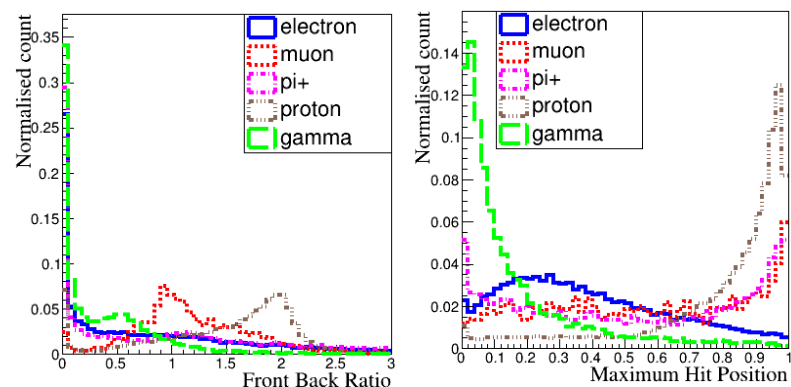
(a) Number of conected tracks. (b) Number of distant tracks. (c) Number of distant clusters.



(d) Length of the primary track. (e) dE/dx of the primary track. (f) Total energy deposit in cone.



(g) Axis max ratio. (h) Truncated max ratio. (i) Q root mean square.



(j) Front back ratio. (k) Maximum hit position.

Figure 5.5. Input variables distribution for EM-shower reconstruction.[17]

Type of variable	variable description
Number of connected tracks	-
Number of distant tracks	-
Number of distant clusters	-
Length of the primary track	-
dE/dx of the primary track	-
Total energy deposit in cone	-
Axis max ratio	A half of the cone apex angle
Truncated max ratio	A charge distribution along the cone axis
Q root mean square	A root mean square of hit charge
Front back ratio	A energy deposit ratio at the front and back of the cone
Maximum hit position	A relative position of the largest charge hit

Table 5.2. Cone variables for EM-shower reconstruction.[17]

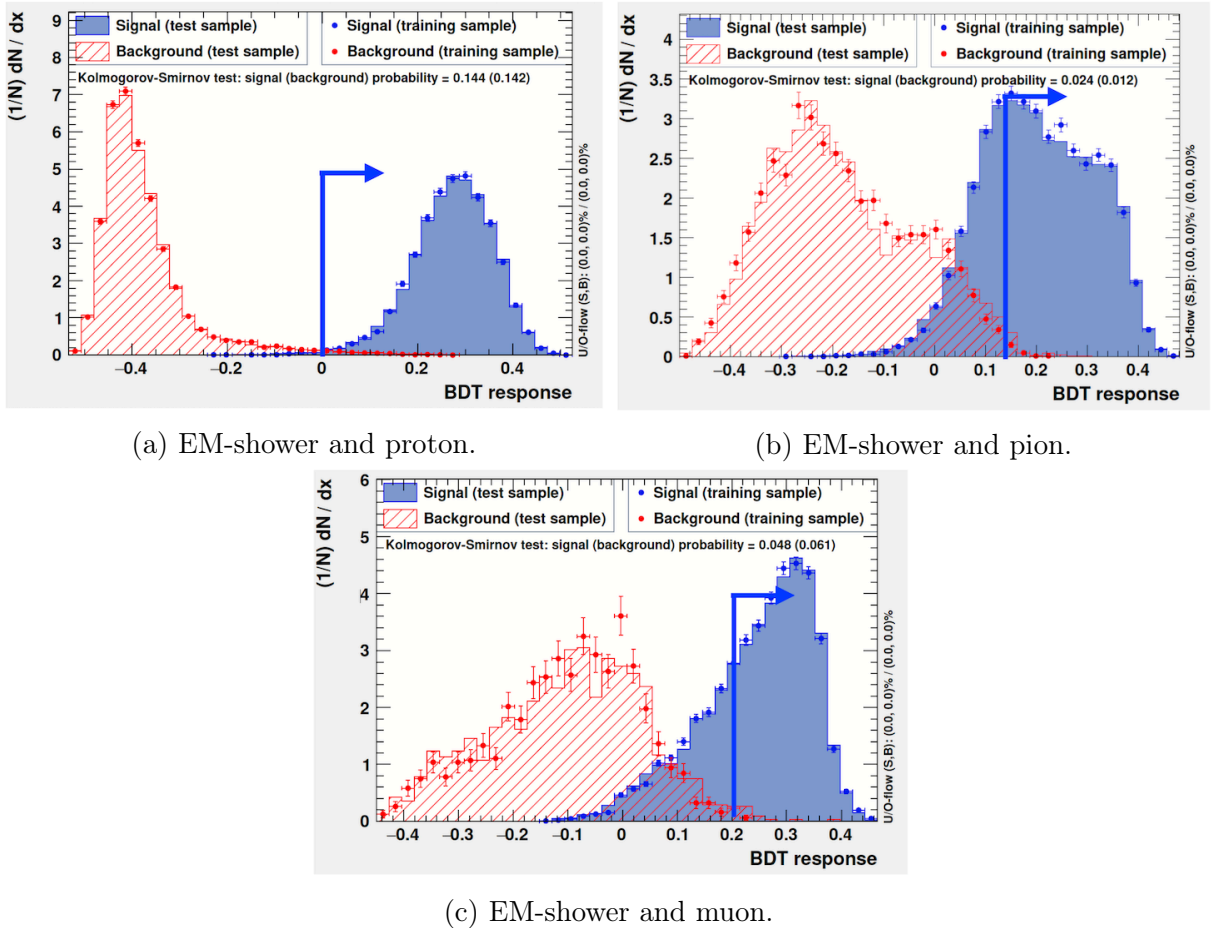


Figure 5.6. GBDT result of EM-shower reconstruction for other particles with particle gun samples[41]. The blue region is EM-shower and the red region is other particles. The blue arrow is the threshold to identify electrons.

Particle	Entries	Identified by EM-shower reconstruction	Identified by TPC&ECal PID	Identified as an electron
p	241345	52	5	57
π^+	58694	50	3	53
π^-	20506	28	2	30
μ^+	6017	4	3	7
μ^-	147614	101	14	115
e^+	36926	355	8	362
e^-	92804	753	215	958
γ	7776	72	12	84
ν_e -CC- e	2483	400	128	521

Table 5.3. The numbers of particles identified by EM-shower reconstruction, TPC and ECal PID, and the two methods combined. The number of ν_e -CC- e contains only ν_e -CC signals in FV. Numbers of e^+ and e^- contain gamma conversion events and external electrons from OOFV. Some particles are identified as electrons by both methods.

5.2.3 TPC and ECal PID

Since the radiation length is about 0.4 m in carbon[15], some electron tracks escape to other detectors from SuperFGD without occurring in an EM shower. Those shower-less tracks whose primary track escapes to other detectors, are identified using TPCs and ECals. The PID likelihood values calculated for each detector are combined TPC and ECal PID likelihood to select an electron-like track as described in Section 4.3.

The result of electron reconstruction is shown in Table 5.3.

5.2.4 Electron/gamma separation

After electron identification, it is necessary to separate whether an electron track and an EM-shower are not produced by gammas.

As a pair track $\gamma \rightarrow e^- + e^+$ has an overlap region, dE/dx around the starting point should be twice as large as for a single electron. Therefore electron is separated from gamma with four types of input variables: Energy deposit at first 15 nodes, Distance and average dE/dx between the primary and second vertex, and Number of connected tracks to the primary track shown as Figure 5.7. The distributions of these input variables for electron/gamma separation are shown in Figure 5.8.

The response of the GBDT method for electron/gamma separation is shown in Figure 5.9. The numbers of electrons identified by electron/gamma separation with GBDT are shown in Table 5.4.

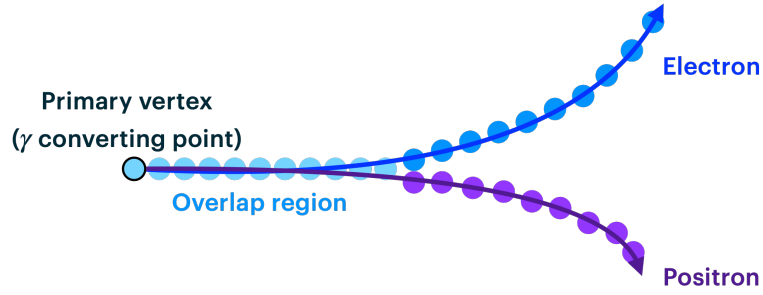


Figure 5.7. A diagram of gamma-ray conversion to electron and positron.

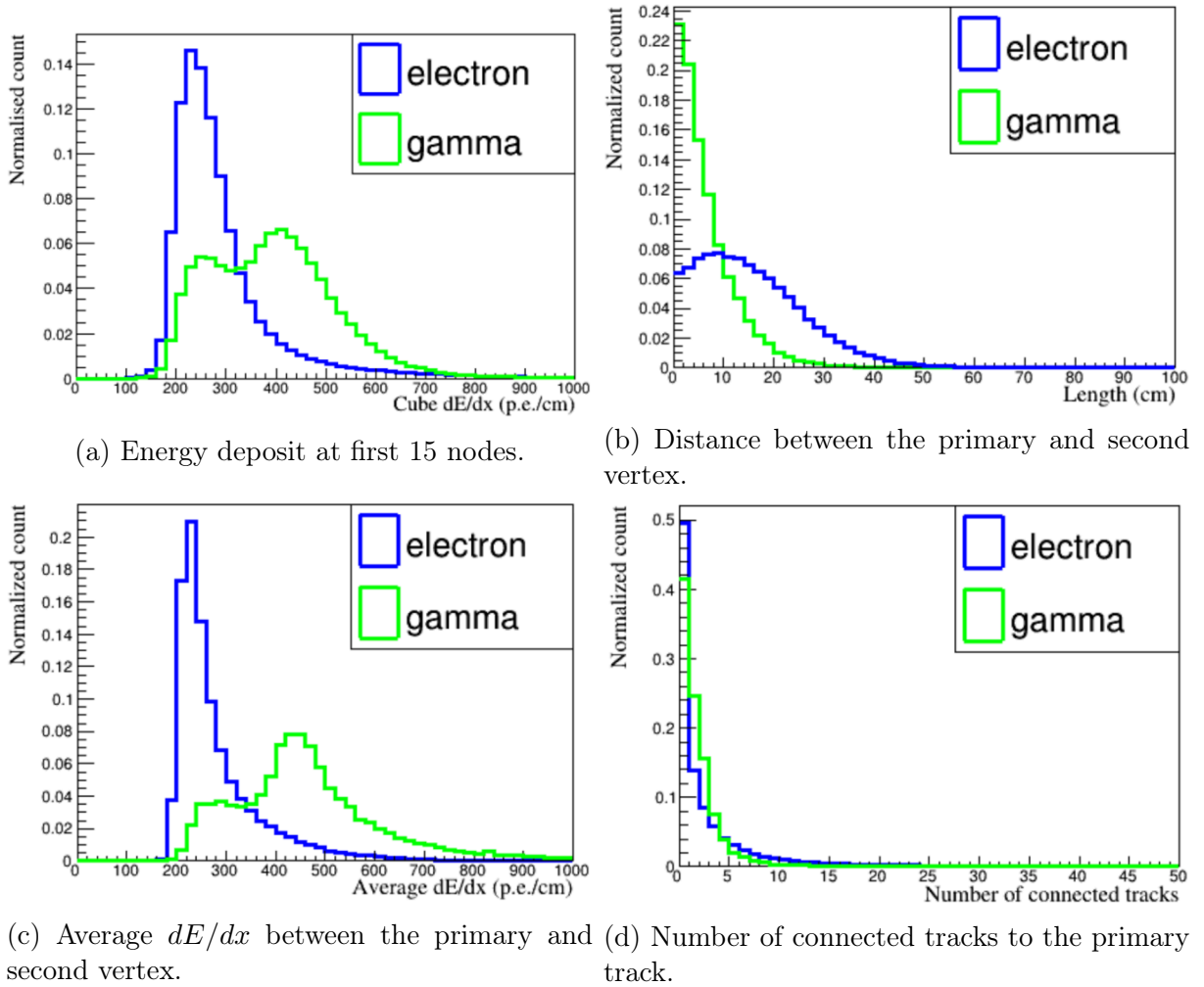


Figure 5.8. Input variables for electron/gamma separation.

Particle	Entries	Identified as an electron by e/γ separation
e^-	958	683
γ	84	43
ν_e CC- e	521	485

Table 5.4. The electron/gamma separation result with NEUT FHC sample.

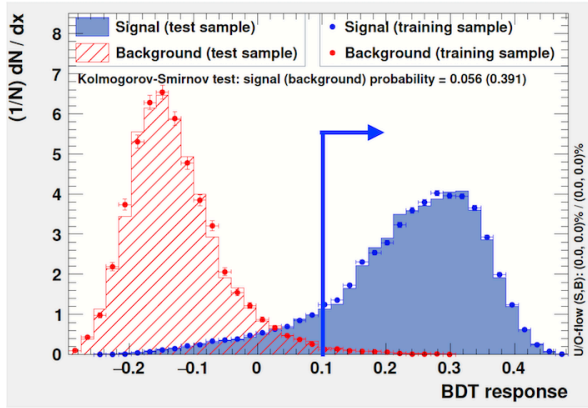


Figure 5.9. GBDT result of electron/gamma separation with particle gun samples[41]. The blue region is electron, and the red region is gamma. The blue arrow is the threshold to identify electrons.

5.3 Other Particle identifications

TPC muon cut

Since some muon neutrino events remain after electron identification, this step is to reject those events by identifying muons. It is difficult to distinguish these particles by TPC PID, as muons and pions have a similar relationship between momentum and energy loss in TPC. However, rejection muons by TPC PID is effective, since about 85.7% of MIP that escape to TPC are muons and about 37% of muons escape each for TPC as shown in Table 5.5. Table 5.6 shows the numbers of neutrino events remaining after applying the TPC muon cut.

	μ^\pm	π^\pm
SuperFGD	21281 (13.6%)	53741(67.5%)
TPC1	58049 (37.0%)	9719(12.2%)
HA-TPC	53738 (34.2%)	11023(13.8%)
Upstream ECal	4371 (2.8%)	2335(2.9%)
Side POD ECal	2809(10.6%)	1323(1.7%)
Other detectors	16674(10.6%)	1450(1.8%)

Table 5.5. The percentage of muons and pions in which detectors they stopped. These particles are produced by neutrino interaction in FV.

Neutrino type	TPC muon cut entries	After muon cut
ν_e -CC	528	483
$\bar{\nu}_e$ -CC	56	51
ν_μ -CC	455	191
$\bar{\nu}_\mu$ -CC	12	6

Table 5.6. The number of neutrino events inside FV cut by TPC muon cut. TPC muon cut is applied to the events that pass the electron/gamma PID.

5.4 Rejection of particles from outside of the fiducial volume

This step is performed to reject events to produce gammas that come from the ECal upstream of SuperFGD. Particles coming from the outside of SuperFGD fiducial volume are rejected by using time information. In particular, neutral particles entering the SuperFGD and interacting inside the fiducial volume become a background.

The timing of the earliest hit in SuperFGD is compared with the timing of the first hit in ECal upstream of SuperFGD. The event is rejected if there is a hit earlier than SuperFGD. By applying this cut, the number of events that interact in upstream ECal is decreased from 50 to 16. Also, since the ECal has $\tilde{5}.0$ ns of time resolution and SuperFGD has $\tilde{1}.5$ ns of time resolution in MC, about 1% of ν_e -CC events are lost in this step.

5.5 Selection result

The inclusive selection performs with a signal purity of 64.1% and an efficiency of 16.7%. The purity is the ratio of the selected ν_e -CC events that interact in SuperFGD FV over the total selected events.

$$\text{purity}_{\nu_e\text{-CC}} = \frac{N_{\text{selected}}^{\nu_e\text{-CC}}}{N_{\text{selected}}^{\nu_e\text{-CC}} + N_{\text{background}}^{\nu_e\text{-CC}}} \quad (5.1)$$

The efficiency is the ratio of the selected ν_e -CC events over the ν_e -CC events with no cuts.

$$\text{efficiency}_{\nu_e\text{-CC}} = \frac{N_{\text{selected}}^{\nu_e\text{-CC}}}{N_{\text{total}}^{\nu_e\text{-CC}}} \quad (5.2)$$

The selected ν_e -CC and total events which pass each selection are shown in Table 5.7. Figure 5.10 shows the transitions of efficiency and purity. A signal efficiency of 75% is lost in the electron PID step since this step requires strict conditions, such as an EM-shower produced within SuperFGD, and an electron entering TPC without an EM-shower. As a result of electron PID, signal purity is increased 45 times more than before this step. Figure 5.11 shows the momentum distribution of selected events.

The selected ν_e -CC inclusive events are 698 events including 449 signal events. As T2K plans to take the neutrino beam data corresponding to 4.0×10^{21} POT data on FHC modes in the next 3 years, the selected ν_e -CC inclusive events will be 2812 events including 1816 signal events. This selection allows us to measure the cross-section on 1816 signal events with $\sqrt{2812/1816} = 2.9\%$ statistical error.

Cut	Selection cut	ν_e -CC	$\bar{\nu}_e$ -CC	$\nu_\mu(\bar{\nu}_\mu)$ -CC	NC	Out of FV	Total events
-	No cut	2701	259	161458	51717	3241775	3458124
0	Pre-cut	2700	257	160966	45218	791231	1000612
1	Vertex selection	2589	235	143080	36146	190625	372708
2	Electron identification	539	63	415	194	431	1650
3	electron/gamma PID	499	49	362	63	163	1141
4	TPC μ cut	454	44	122	46	125	791
5	Rejection of OOFV	449	44	114	44	47	698

Table 5.7. Summary of ν_e -CC selection showing the numbers of ν_e -CC, backgrounds and total events which pass each selection cut.

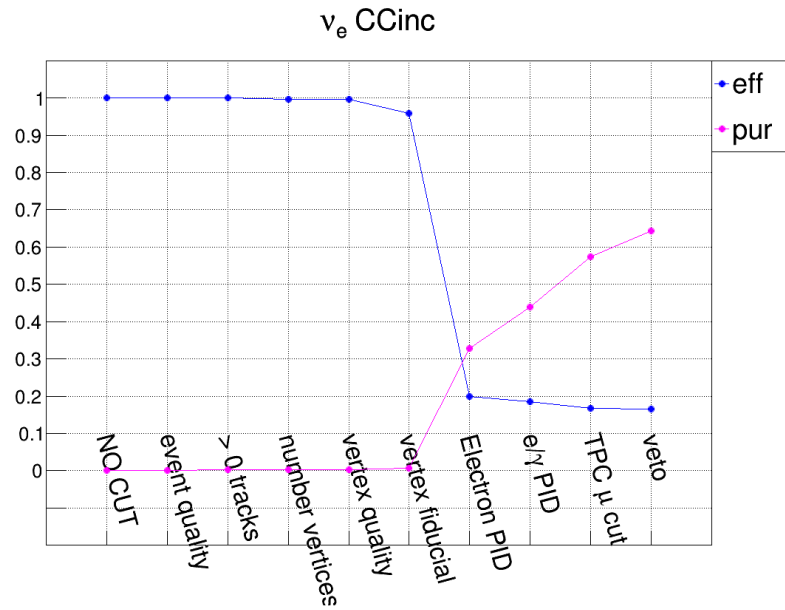


Figure 5.10. Transitions of the purity(pink line) and efficiency(blue line).

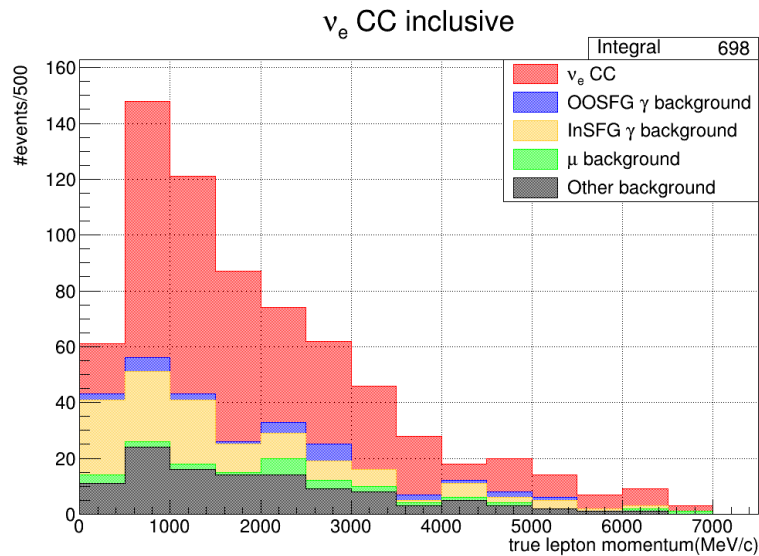
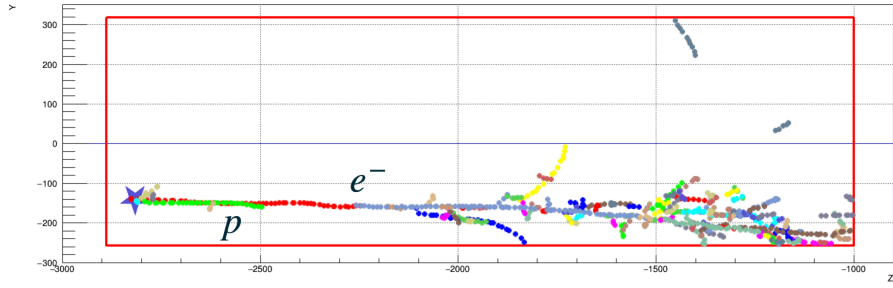
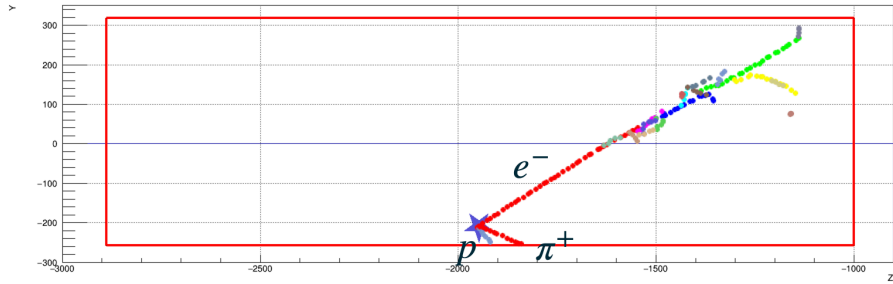


Figure 5.11. A momentum distribution of selected events.



(a) A ν_e -CCQE mode.



(b) A ν_e -CCRes $1\pi^+$ mode.

Figure 5.12. The event displays of selected as ν_e -CC events(SuperFGD side view). The red rectangle is the SuperFGD area. Each color-coded line represents a reconstructed track, and the blue star is a selected vertex.

5.5.1 Selected ν_e -CC events

The numbers of ν_e -CC interaction modes are in Table 5.8. The most dominant mode is ν_e -CCQE interaction which accounts for 43.6% of the total ν_e -CC events. The second most dominant mode is ν_e -CCRes interaction which accounts for 34.5% of the total ν_e -CC events. The event displays of the selected events whose modes are CCQE and CCRes are shown in Figure 5.12.

5.5.2 Selected background events

The number of background events categories are shown in Table 5.9. The dominant backgrounds are the gamma, ν_μ -CC DIS, and $\bar{\nu}_e$ background. Gamma backgrounds are separated by where gamma is produced: in FV(γ -FV) and out of FV(γ -OOFV). About 80.9% of the gamma background comes from π^0 decay as shown in Table 5.10. The gamma background corresponds to 45.8% of the background events since an EM-shower generated from the gamma-ray is misidentified as an electron EM-shower.

Also, the structure of particle jets generated by ν_μ -CC DIS interaction mimics EM-shower and is misidentified as an electron EM-shower.

Interaction mode	
CCQE	193
2p2h	32
Res	155
DIS	67
Coh	2
total	449

Table 5.8. The number of events divided by interaction mode for signal events

Background	
ν_μ -CCQE	4
ν_μ -2p2h	0
ν_μ -Res	9
ν_μ -DIS	39
ν_μ -Coh	0
ν_μ -NC	15
$\bar{\nu}_e$	42
$\bar{\nu}_\mu$	3
γ -FV	84
γ -OOFV	30
Out of FV	23
total	249

Table 5.9. The number of background events.

Gamma source	FV	OOFV
CC- γ	9	8
NC- γ	4	1
CC-N π^0	49	15
NC-N π^0	22	6

Table 5.10. The number of events by gamma background source. CC and NC- γ produce gammas from interaction without π^0 . CC/NC-N π^0 produces π^0 which decay to gammas.

Chapter 6

Classification of ν_e -CC events

6.1 Classification based on final states

The ν_e -CC candidate events selected in Chapter 5 are classified based on the numbers of charged pions and protons as shown in Figure 6.1. First, events are categorized into $CC0\pi^\pm$, $CC1\pi^\pm$, and $CC\text{multi-}\pi^\pm$ samples based on the number of reconstructed charged pions. Then, based on the number of reconstructed protons, $CC0\pi^\pm$ events are further divided into $CC0\pi^\pm 0p$, $CC0\pi^\pm 1p$, and $CC0\pi^\pm \text{multi-}p$ samples, and $CC1\pi^\pm$ are divided into $CC1\pi^\pm 0p$, $CC1\pi^\pm 1p$ and $CC1\pi^\pm \text{multi-}p$ samples. Pions are identified by applying pion PID described in Chapter 4. Among proton-like tracks found in vertex selection, those starting positions within 30 mm from the vertex are counted as protons. The numbers of protons and pions are shown in Table 6.1. The 52.3% of protons and 51.3% of pions are reconstructed.

	Number of true particle	Selected events	Correct	Miss-identified
Proton PID	736	436	390	46
Pion PID	337	342	173	171

Table 6.1. Number of particles identified as protons and pions. This shows the total selected events: selected events correctly and incorrectly (miss-identified).

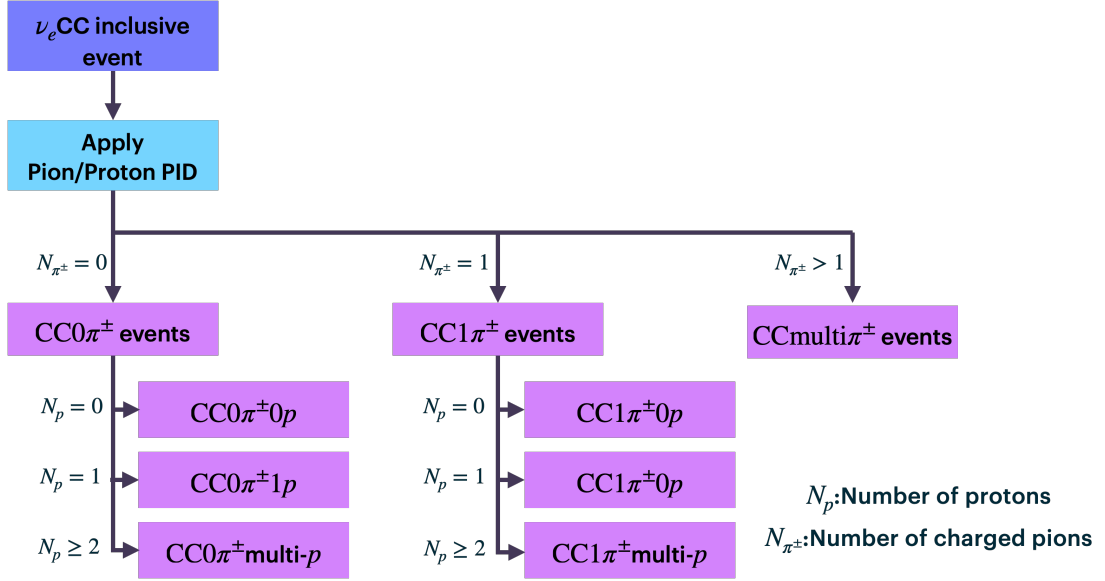


Figure 6.1. Event sample classification flow of ν_e -CC interaction based on the final states.

6.2 Study of background reduction for ν_e -CC inclusive event selection

The classification result is shown in Table 6.2. Momentum distributions of $CC0\pi^\pm$ and $CC1\pi^\pm$ samples are shown in Figure 6.3. Comparing the three samples, the $CC0\pi^\pm$ samples are selected with higher purity than other samples. In particular, the set of $CC0\pi^\pm 1p$ and $CC0\pi^\pm \text{multi-}p$ samples is selected with a purity of 79.6%. Since the other samples are selected with a purity lower than the inclusive ones, the background reduction in $CC0\pi^\pm 0p$, $CC1\pi^\pm$, and $CC\text{multi}\pi^\pm$ samples is important to achieve a higher purity inclusive selection.

Figure 6.2 shows three types of major background: γ , $\bar{\nu}_e$, and ν_μ background. The details of these backgrounds for each sample are followings.

Sample	ν_e -CC	γ	$\bar{\nu}_e$	$\nu_\mu(\bar{\nu}_\mu)$	OOFV	Total bkg.	Total events	Efficiency	Purity
CC-inclusive	449	114	42	70	23	249	698	16.7%	64.1%
$CC0\pi^\pm$	308	52	33	31	11	127	433	11.4%	71.1%
$CC0\pi^\pm 0p$	117	37	19	13	8	77	192	-	60.9%
$CC0\pi^\pm 1p$	150	13	11	16	2	42	192	-	78.1%
$CC0\pi^\pm \text{multi-}p$	41	2	3	2	1	8	49	-	83.7%
$CC1\pi^\pm$	119	44	8	28	7	87	205	4.4%	58.0%
$CC1\pi^\pm 0p$	64	23	7	19	5	54	119	-	53.7%
$CC1\pi^\pm 1p$	40	18	1	4	2	25	63	-	60.3%
$CC1\pi^\pm \text{multi-}p$	15	1	0	5	0	8	23	-	63.5%
$CC\text{multi}\pi^\pm$	22	18	1	11	5	35	60	-	36.7%

Table 6.2. The number of ν_e -CC events and background(bkg.), the signal efficiency, and the signal purity for each sample.

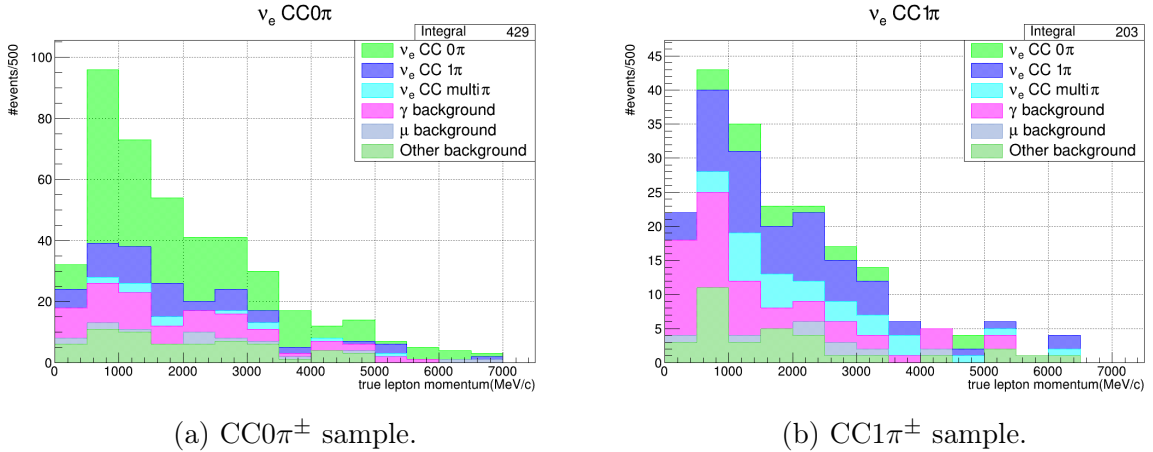


Figure 6.2. The momentum distribution of selected electron-neutrino events with a charged pion for stacked each category which is defined by the number of MC true particles.

6.2.1 γ background

Gamma background is the dominant background in all of $CC0\pi^\pm 0p$, $CC1\pi^\pm$, and $CC\text{multi}\pi^\pm$ samples. In $CC0\pi^\pm$ samples, as the fraction of background decreases when proton tracks are required, the improvement of proton detection efficiency leads to gamma background rejection in the $CC0\pi^\pm 0p$ sample. On the contrary, the fraction of background does not change significantly if protons are required in the $CC1\pi^\pm$ sample. This no-change is due to two conditions as follows in $CC1\pi^\pm$ and $CC\text{multi}\pi^\pm$ samples.

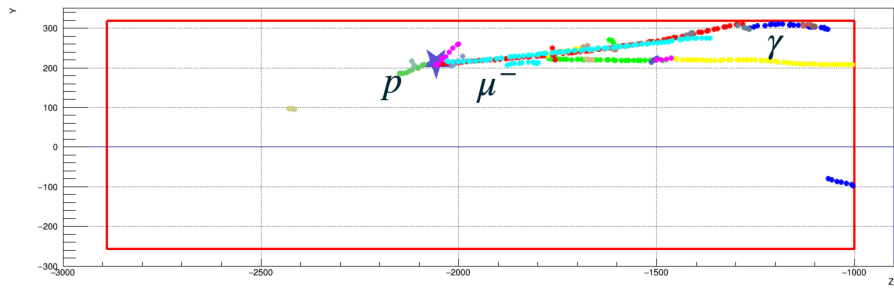
- A gamma and a muon generated by ν_μ -CC interaction are misidentified as an electron and a charged pion, respectively.
- Most ν_μ -CC gamma productions generate a proton via CCRes and CCDIS interaction modes.

Also, there are many backgrounds in the low momentum region of lepton in the $CC1\pi^\pm$ sample as shown in Figure 6.3. Thus, the following two approaches are considered to be effective in reducing gamma background.

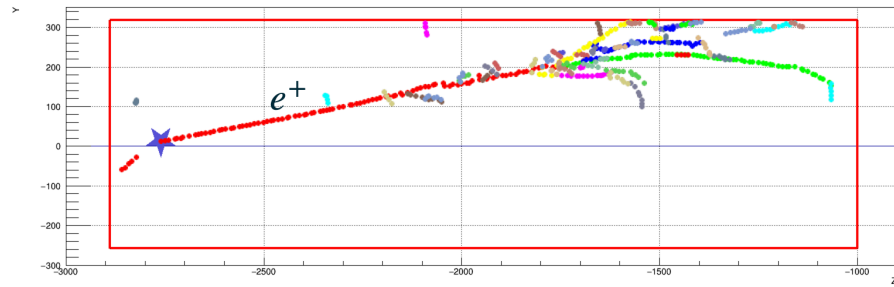
- Identification of low momentum muon tracks to reject ν_μ - γ productions. It requires discrimination of muons from pions with SuperFGD PID because low-momentum muons tend to stop inside SuperFGD.
- Improvement of electron/gamma separation in low momentum region.

6.2.2 $\bar{\nu}_e$ background

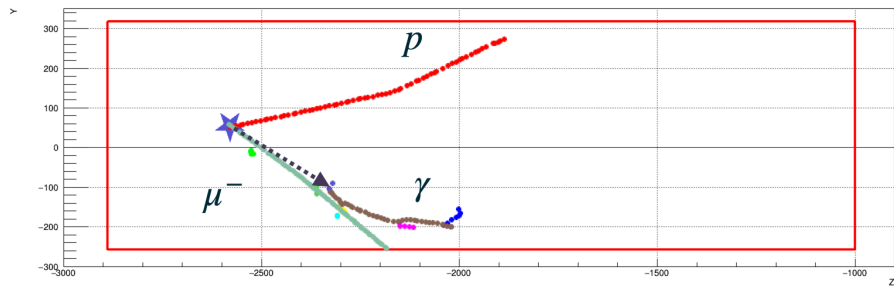
The 61.9% of $\bar{\nu}_e$ background which generates a positron is classified into $CC0\pi^\pm 0p$ and $CC1\pi^\pm 0p$ samples because most $\bar{\nu}_e$ interactions do not produce protons. The background is due to the lack of identification of particle charges in the EM shower reconstruction. To reduce this background, it is necessary to identify the charge of the EM shower to discriminate between an electron and a positron.



(a) A γ background.



(b) A $\bar{\nu}_e$ background.



(c) A ν_μ background. The dotted arrow is the path gamma took without gamma conversion.

Figure 6.3. The event displays of the major background events (SuperFGD side view). The red rectangle is the SuperFGD area. Each color-coded line represents a reconstructed track, and the blue star is a selected vertex.

ν_μ interaction mode	CC0 π^\pm	CC1 π^\pm	CCmulti π^\pm
ν_μ -CCQE	4	0	0
ν_μ -CCRes	6	3	9
ν_μ -CCDIS	11	19	2
ν_μ -NC	2	5	0
Total ν_μ events	31	28	11

Table 6.3. The number of ν_μ background which are categorized by interaction mode for each sample.

6.2.3 ν_μ background

In the CC1 π^\pm and CCmulti π^\pm samples, the ν_μ event without gammas identified as electrons in the final state. In particular, these backgrounds come from the ν_μ -CCRes and ν_μ -CCDIS interaction mode as shown in Table 6.3. Since these interactions produce multiple particles in addition to a lepton and a proton, this background is mainly caused by the multiple particles reconstructed as an EM-shower. In addition to the improvement of muon identification, improvement of cone construction can reduce such background. While multiple tracks are produced near the vertex in the ν_μ -CCRes and ν_μ -CCDIS modes, EM-showers occur in the middle of the electron tracks. It may be possible to discriminate them by checking whether the tracks within a cone originate from near the vertex.

6.3 Study of the exclusive final state selection for cross-section measurement

For the measurement of exclusive mode, the classification results are evaluated as the sample for the MC true signals which are categorized by the number of MC true particles. For instance, the purity and efficiency of CC0 π^\pm are defined as,

$$\text{purity}^{\text{CC0}\pi^\pm} = \frac{N_{\text{selected}}^{\text{CC0}\pi^\pm\text{signal}}}{N_{\text{selected}}^{\text{CC0}\pi^\pm\text{signal}} + N_{\text{selected}}^{\text{background}}}, \quad (6.1)$$

$$\text{efficiency}^{\text{CC0}\pi^\pm} = \frac{N_{\text{selected}}^{\text{CC0}\pi^\pm\text{signal}}}{N_{\text{no cut}}^{\text{CC0}\pi^\pm\text{signal}}}. \quad (6.2)$$

The summary of the selection for ν_e -CC exclusive event samples is shown in Table 6.4. The result of each selected event is explained in the following.

6.3.1 The CC0 π^\pm sample

The selected CC0 π^\pm events are 433 events including 262 signals and the selection performs with a signal purity of 60.5% and an efficiency of 17.1%. This sample contains the 90.7% of CC0 π^\pm signals before the classification.

Selected sample	Selected events	CC0 π^\pm (True)	CC1 π^\pm (True)	CCmulti π^\pm (True)	Other bkg.	Efficiency	Purity
CC0 π^\pm	433	262	41	5	125	17.1%	60.5%
CC1 π^\pm	205	23	78	18	86	9.3%	38.0%
CCmulti π^\pm	60	4	10	8	38	2.4%	13.3%
Total	698	289	129	31	249		

Table 6.4. The number of classified events categorized by ν_e -CC samples and the other background and signal efficiency/purity for ν_e -CC exclusive events. "(True)" means the number of events categorized by the MC true number of pions. The numbers in bold are the number matches between sample and true

This selection can collect 1751 events including 1059 signal events in the next three years. It has the capability of cross-section measurement with $\sqrt{1751}/1059 = 4.0\%$ statistical uncertainty.

The 26.9% of the backgrounds is the ν_e -CC pion production with no reconstructed charged pions. To get the higher purity value, it is necessary to increase the reconstruction efficiency of pions in ν_e -CC events.

6.3.2 The CC1 π^\pm sample

The selected CC1 π^\pm events are 205 events including 78 signals and the selection performs with a signal purity of 38.0% and an efficiency of 9.3%. This sample contains the 60.5% of CC1 π^\pm signals before the classification. This selection can collect 829 events including 315 signal events in the next three years. It has the capability of cross-section measurement with $\sqrt{829}/315 = 9.1\%$ statistical uncertainty. Also, this selection can collect 263 events including 65 signal events with $\sqrt{263}/65 = 24.9\%$ statistical uncertainty in the energy range of leptons under the 1 GeV/c as measured in SK.

The gamma is the large background in the low momentum range as shown in Figure 6.3. The gamma rejection needs to be improved as described in Section 6.2. Also, the improvement of the pions reconstruction in the low momentum region is necessary to get higher efficiency.

6.3.3 The selected CCmulti π^\pm events

The 60 events are selected as CCmulti π^\pm events, but this is a small statistic to measure this sample.

Chapter 7

Discussion

7.1 Impacts on T2K oscillation analysis

In the T2K oscillation analysis, the cross-section of the ν_e -CC interaction has 3.0% systematic uncertainties. This thesis describes the ν_e -CC inclusive cross-section that can be measured with 2.9% of the statistical uncertainty using T2K neutrino beam data in the next three years. Since this result does not consider the systematic uncertainties in the cross-section measurement, this does not significant impact on reducing the ν_e CC cross-section uncertainties. However, this result indicates that upgraded ND280 has the potential to measure ν_e -CC cross-sections towards the reduction of the systematic uncertainty. Also, this thesis shows the background composition and the improvements for the background events reduction and indicates the possibility of the selection of ν_e -CC events with higher purity.

In the ν_e -CC exclusive selection, the $CC0\pi^\pm$ sample can be measured with 4.0% statistical uncertainty, and the $CC1\pi^\pm$ sample can be measured with 9.1% statistical uncertainty. Thus, the upgraded ND280 has the capability of the cross-section measurement of the exclusive samples. In the energy range of leptons under the 1 GeV/c, the $CC1\pi^\pm$ sample can be measured with 24.9% statistical uncertainty. This uncertainty is smaller than the $CC1\pi$ excess amount of 40% in SK. However, since the uncertainty of the number of background events is large, background rejection in this energy region is needed to investigate $CC1\pi$ excess in ND280. Reducing the background in this result allows comparison between MC samples and real data and verifies the MC simulation which is also used in the oscillation analysis.

7.2 Future improvements

Gamma rejection

Improvement of proton reconstruction and electron/gamma separation in the low-momentum range can further reduce the gamma background. In the current selection algorithm, four nodes around the interaction vertex are ignored to avoid overlap effects from multiple tracks. The energy deposit around the vertex needs to be used for the reconstruction of protons and the electron/gamma separation with a short track. Also, gamma may be

rejected by calculating the invariant mass of $e^- + e^+$ pair track as it was performed in the original ND280 analysis[7].

Particle charge identification to reject positron

To reduce the positron background, the charge identification of the EM-shower is necessary using a cone object such as comparing the primary track and center of the shower.

Muon identification

In this thesis, muons are rejected by only TPC PID. Since there are muons not to enter the TPC, they have to be rejected by SuperFGD PID. However, energy deposit patterns of muons are similar to that of pions. The algorithm to reject only muons needs to be developed. Also, HA-TPC PID should be developed and implemented.

Cone construction

To reduce the background of multiple tracks mimicking EM-shower, the cone reconstruction can be improved by checking whether the tracks within a cone originate from near the vertex.

Charged pion identification

To reconstruct low-momentum $CC1\pi^\pm$ samples, the pions identification method needs to be improved with additional information, such as Michel electron.

Selection with HA-TPCs and TOF

This thesis does not use the reconstructed HA-TPC and TOF tracks. The development of the selection with HA-TPCs and TOF is necessary to evaluate realistic performance and it will improve performances such as particle identification.

Chapter 8

Summary

The T2K(Tokai-to-Kamioka) experiment is a long baseline neutrino oscillation experiment in Japan. T2K aims to observe CP violation in the lepton sector. Until now, T2K has excluded CP conservation in neutrino oscillations with more than a 90% confidence level. The uncertainty on the ν_e cross-section is 3.0% of the predicted number of ν_e -CC events in the Super-Kamiokande. To achieve higher precision, we are upgrading each component and are about to start the T2K-II phase. To reduce the systematic uncertainties in the oscillation analysis, ND280 is upgraded and we have developed selection algorithms with upgraded ND280 for the electron neutrino interactions using Monte Carlo simulation.

At the present in 2024, the ν_e -CC events can be selected with an efficiency of 16.7% and a purity of 64.1%. The result demonstrates the capability to collect the 2812 candidate events including 1816 signal events in the next three years which allows the ν_e -CC measurement with $\sqrt{2812}/1816 = 2.9\%$ statistical uncertainty. As a result of the classification of the electron neutrino events based on their final states, $CC0\pi^\pm 0p$, $CC1\pi^\pm$, and $CC\text{multi-}\pi^\pm$ samples had large background contamination. This thesis searched for the improvement in reducing the background for each event sample. This improvement is expected to increase the capability of the impact on oscillation analysis.

Also, measurement of cross-sections in specific final states may be possible in the future. The $CC0\pi^\pm$ events are selected with the efficiency and purity of 17.1% and 60.5%, respectively. The efficiency and purity for the $CC1\pi^\pm$ events are 9.3% and 38.0%, respectively. Based on the results of this study, possible improvements were discussed.

Acknowledgment

I would like to express my special thanks to my supervisor, Prof. Masashi Yokoyama for giving me such an opportunity to conduct my research. I also would like to thank Prof. Yasuhiro Nakajima and Prof. Kota Nakagiri for their support during my master's course and helpful advice. I wish to thank Eguchi-san too. He gave me a lot of advice for my analysis. I want to express my special gratitude to the members of the Yokoyama-Nakajima Laboratory at the University of Tokyo, Daniel, Yoshimi, Kodama-san, Wataru Okinaga, Eiichirou Watanabe, Arai-kun, Goto-kun, Mizuno-kun, Muro-kun, and Kono-san. I received a lot of advice and support which are related not only to physics but also to daily life.

I appreciate the support and feedback from the members of the Analysis Development group in T2K, Davide Sgalaberna, Lorenzo Magaletti, Mathieu Guigue, Clark McGrew, Xingyu Zhao, and Weijun Li. It was always helpful to discuss with them about the analysis.

I also want to thank the members of the T2K collaboration, especially Matsubara-san, Kikawa-san, Tanigawa-san, Abe-san, Arihara-san, Kawaue-san, Takumi Tsushima, and Yusuke Furui.

Finally, I would like to show my special appreciation to my family for all the kind support they gave me.

List of Figures

1.1	Muon-neutrino cross sections of neutrino-nucleus interactions in ^{12}C . The shaded area is the expected neutrino beam flux in T2K.[1]	7
1.2	A diagram of CCQE.[2]	7
1.3	A diagram of CCRes single pion production.[2]	8
1.4	A diagram of CCDIS.[2]	8
1.5	A diagram of CCcoh.[2]	8
2.1	A T2K overview.[16]	10
2.2	Overview of J-PARC accelerators.[17]	12
2.3	Left: overview of neutrino beamline. Right: side view of the secondary beamline.[18]	12
2.4	The predicted flux as a function of neutrino energy at ND280 in FHC mode.[7]	13
2.5	The neutrino oscillation probability and muon neutrino flux in T2K neutrino beam.[19]	14
2.6	Overview of ND280.[18]	15
2.7	A structure of FGD sub-module.[21]	15
2.8	A schematic view of Super-Kamiokande.[23]	16
2.9	Event displays of Cherenkov rings. Left: muon-like, right: electron-like.[18]	17
2.10	The $\Delta\chi^2$ distribution in δ_{CP} from fitting to the data with reactor constraint applied. The shaded confidence intervals are calculated using the Feldman-Cousins method.[24]	18
2.11	The events for the $1e1de$ SK samples, shown in reconstructed electron momentum and the angle between the neutrino beam and the lepton in the lab frame. The insets show the events projected onto each single dimension, and the red line is the expected number of events.[24]	19
2.12	The reconstructed momentum distributions of ν_e -CC candidates for FHC mode(Left) and RHC mode(Right).[7]	20
3.1	A schematic view of the upgraded ND280 and coordinate axis.[27]	23
3.2	A schematic view of the SuperFGD.[27]	23
3.3	The conceptual drawing of the light injection method for a large number of channels and a picture of the LGP prototype.[31]	24
3.4	A schematic view of the HA-TPC.[27]	25
3.5	A layout of the TOF.[27]	25

3.6	The muon tracking efficiency as a function of the cosine of the angle with respect to the z axis (θ). The purple line is the original ND280 configuration. The blue line is the upgraded configuration with muons in TPC only, also the green line includes the muons stopping SuperFGD.[32]	26
3.7	Expected track reconstruction efficiencies for pions(left) and protons(right) in SuperFGD with three readout views or with only two readout views.[27]	26
3.8	The situations of SuperFGD construction	28
3.9	A display of the database system(Left) and the situation to register MPPC to the database system with iPad[33](Right).	28
4.1	Input detector geometries for Geant4 simulation(side view).	32
4.2	The flow of detector response simulation for SuperFGD.	32
4.3	The flow of reconstruction algorithms for SuperFGD.	33
4.4	Kink finding method. The green squares are sub-sequence hits scanned. The orange line is the distance of the middle hit from the line between the two end hits.[17]	33
4.5	Node energy patterns of particle gun sample in SuperFGD. Only particles stopping in SuperFGD are considered. The "w/ Bragg" and "w/o Bragg" mean particles stopping with Bragg peak or without Bragg peak due to interacting with nucleons.[40]	34
4.6	GBDT result of each particle based on track in SuperFGD.[40]	35
4.7	Energy loss in the TPC of tracks starting from FGD1 in real data. Left: negatively charged tracks. Right: positively charged tracks. Each curve shows the expected energy loss curves for electrons, muons, pions, and protons.[7]	35
4.8	Performance of the ECal PID using samples of cosmic and through-going muons, electrons, positrons from gamma conversions, and protons from neutrino interactions. Left: Log-likelihood ratio of the ECal track-shower ($R_{MIP/EM}$) PID. Right: Log-likelihood ratio of the ECal electron-proton ($R_{EM/HIP}$) PID for showers with $R_{MIP/EM} > 0$ and the momentum larger than 600 MeV/c. Plots are normalized to unity.[7]	36
4.9	Momentum distribution of MC true and reconstructed particles. Red histogram shows the momentum distribution of the MC true, green histogram shows the momentum distribution of the reconstructed particle whose type is correctly identified. This distribution does not include misidentified types of particles.	37
5.1	Algorithm flows of ν_e -CC inclusive selection.	39
5.2	Distribution of the distance between true and selected vertex. The red area is ν_e -CCQE events and the blue area is not ν_e -CCQE events. The histograms are stacked.	40
5.3	Algorithm flow for electron track detection.	41
5.4	A schematic view of a cone object. Blue: primary track, purple: connected tracks, light green: distant tracks, and light blue: cone.	41
5.5	Input variables distribution for EM-shower reconstruction.[17]	42

5.6	GBDT result of EM-shower reconstruction for other particles with particle gun samples[41]. The blue region is EM-shower and the red region is other particles. The blue arrow is the threshold to identify electrons.	43
5.7	A diagram of gamma-ray conversion to electron and positron.	45
5.8	Input variables for electron/gamma separation.	45
5.9	GBDT result of electron/gamma separation with particle gun samples[41]. The blue region is electron, and the red region is gamma. The blue arrow is the threshold to identify electrons.	46
5.10	Transitions of the purity(pink line) and efficiency(blue line).	48
5.11	A momentum distribution of selected events.	48
5.12	The event displays of selected as ν_e -CC events(SuperFGD side view). The red rectangle is the SuperFGD area. Each color-coded line represents a reconstructed track, and the blue star is a selected vertex.	49
6.1	Event sample classification flow of ν_e -CC interaction based on the final states.	52
6.2	The momentum distribution of selected electron-neutrino events with a charged pion for stacked each category which is defined by the number of MC true particles.	53
6.3	The event displays of the major background events (SuperFGD side view). The red rectangle is the SuperFGD area. Each color-coded line represents a reconstructed track, and the blue star is a selected vertex.	54

List of Tables

1.1	Published measurements of electron neutrino and antineutrino cross sections from modern accelerator-based neutrino experiments.[15]	9
2.1	The systematic uncertainty on predicted relative number of ν_e and $\bar{\nu}_e$ candidates in the Super-Kamiokande with no decay electrons.[25]	18
2.2	Expected and observed number of neutrino-events at SK	19
4.1	Number of simulated neutrino interaction events.	31
4.2	Number of events for ν_e -CC interaction types categorized by the number of pions and protons in the final state. The multi- p requires two or more protons, the multi- π^\pm requires a total of two or more π^\pm and π^- .	31
4.3	The characteristics of the particle gun samples	31
4.4	Input variables for GBDT to identify particles based on track in SuperFGD.	34
5.1	The performance of the vertex selection in ν_e -CCQE mode by methods of only 2-(a), and combined 2-(a) and 2-(b). The detection ratio is the ratio of detecting vertex inside SuperFGD. The 30 mm-ratio is the ratio that a vertex is selected within 30 mm from the position of the MC true vertex.	40
5.2	Cone variables for EM-shower reconstruction.[17]	43
5.3	The numbers of particles identified by EM-shower reconstruction, TPC and ECal PID, and the two methods combined. The number of ν_e -CC- e contains only ν_e -CC signals in FV. Numbers of e^+ and e^- contain gamma conversion events and external electrons from OOFV. Some particles are identified as electrons by both methods.	44
5.4	The electron/gamma separation result with NEUT FHC sample.	45
5.5	The percentage of muons and pions in which detectors they stopped. These particles are produced by neutrino interaction in FV.	46
5.6	The number of neutrino events inside FV cut by TPC muon cut. TPC muon cut is applied to the events that pass the electron/gamma PID.	47
5.7	Summary of ν_e -CC selection showing the numbers of ν_e -CC, backgrounds and total events which pass each selection cut.	48
5.8	The number of events divided by interaction mode for signal events	50
5.9	The number of background events.	50
5.10	The number of events by gamma background source. CC and NC- γ produce gammas from interaction without π^0 . CC/NC-N π^0 produces π^0 which decay to gammas.	50

6.1	Number of particles identified as protons and pions. This shows the total selected events: selected events correctly and incorrectly(miss-identified).	51
6.2	The number of ν_e -CC events and background(bkg.), the signal efficiency, and the signal purity for each sample.	52
6.3	The number of ν_μ background which are categorized by interaction mode for each sample.	55
6.4	The number of classified events categorized by ν_e -CC samples and the other background and signal efficiency/purity for ν_e -CC exclusive events. "(True)" means the number of events categorized by the MC true number of pions. The numbers in bold are the number matches between sample and true	56

Bibliography

- [1] Naruhiro Chikuma. *Measurements of neutrino charged-current interactions on water and hydrocarbon targets using a sub-GeV anti-neutrino beam*. PhD thesis, Department of Physics, Graduate School of Science The University of Tokyo, 2018. (pages 7, 61).
- [2] Taichiro Koga. *Measurement of neutrino interactions on water and search for electron anti-neutrino appearance in the T2K experiment*. PhD thesis, Department of Physics, Graduate School of Science The University of Tokyo, 2018. (pages 7, 8, 61).
- [3] M. Martini M. Ericson G. Chanfray and J. Marteau. Unified approach for nucleon knock-out and coherent and incoherent pion production in neutrino interactions with nuclei. *Physical review C*, 80, 12 2009. doi:10.1103/PhysRevC.80.065501. (page 9).
- [4] J. Nieves I. Ruiz Simo and M. J. Vicente Vacas. Inclusive charged-current neutrino-nucleus reactions. *Physical review C*, 83, 4 2011. doi:10.1103/PhysRevC.83.045501. (page 9).
- [5] K. Abe et al. Measurement of the Inclusive Electron Neutrino Charged Current Cross Section on Carbon with the T2K Near Detector. *Physical Review Letters*, 113, 12 2014. 241803. doi:10.1103/PhysRevLett.113.241803. (pages 9, 19).
- [6] K. Abe et al. Measurement of the electron neutrino charged-current interaction rate on water with the t2k nd280 π^0 detector. *Phys. Rev. D*, 91:112010, Jun 2015. URL: <https://link.aps.org/doi/10.1103/PhysRevD.91.112010>, doi:10.1103/PhysRevD.91.112010. (pages 9, 19).
- [7] K. Abe et al. Measurement of the charged-current electron (anti-)neutrino inclusive cross-sections at the T2K off-axis near detector ND280. *JHEP*, 10:114, 2020. arXiv: 2002.11986, doi:10.1007/JHEP10(2020)114. (pages 9, 13, 19, 20, 35, 36, 58, 61, 62).
- [8] R. Acciarri et al. First measurement of electron neutrino scattering cross section on argon. *Phys. Rev. D*, 102:011101, Jul 2020. URL: <https://link.aps.org/doi/10.1103/PhysRevD.102.011101>, doi:10.1103/PhysRevD.102.011101. (page 9).
- [9] P. An et al. Measurement of electron-neutrino charged-current cross sections on ^{127}I with the coherent NaI ν E detector. *Phys. Rev. Lett.*, 131:221801, Nov 2023. URL: <https://link.aps.org/doi/10.1103/PhysRevLett.131.221801>, doi: 10.1103/PhysRevLett.131.221801. (page 9).

- [10] P. Abratenko et al. Measurement of the flux-averaged inclusive charged-current electron neutrino and antineutrino cross section on argon using the numi beam and the microboone detector. *Phys. Rev. D*, 104:052002, Sep 2021. URL: <https://link.aps.org/doi/10.1103/PhysRevD.104.052002>, doi: 10.1103/PhysRevD.104.052002. (page 9).
- [11] P. Abratenko et al. First measurement of inclusive electron-neutrino and antineutrino charged current differential cross sections in charged lepton energy on argon in microboone. *Phys. Rev. D*, 105:L051102, Mar 2022. URL: <https://link.aps.org/doi/10.1103/PhysRevD.105.L051102>, doi:10.1103/PhysRevD.105.L051102. (page 9).
- [12] P. Abratenko et al. Differential cross section measurement of charged current ν_e interactions without final-state pions in microboone. *Phys. Rev. D*, 106:L051102, Sep 2022. URL: <https://link.aps.org/doi/10.1103/PhysRevD.106.L051102>, doi: 10.1103/PhysRevD.106.L051102. (page 9).
- [13] J. Wolcott et al. Measurement of electron neutrino quasielastic and quasielasticlike scattering on hydrocarbon at $\langle E_\nu \rangle = 3.6$ GeV. *Phys. Rev. Lett.*, 116:081802, Feb 2016. URL: <https://link.aps.org/doi/10.1103/PhysRevLett.116.081802>, doi:10.1103/PhysRevLett.116.081802. (page 9).
- [14] M. A. Acero et al. Measurement of the ν_e -nucleus charged-current double-differential cross section at $\langle E_\nu \rangle = 2.4$ GeV using nova. *Phys. Rev. Lett.*, 130:051802, Feb 2023. URL: <https://link.aps.org/doi/10.1103/PhysRevLett.130.051802>, doi: 10.1103/PhysRevLett.130.051802. (page 9).
- [15] R. L. Workman and Others. Review of Particle Physics. *PTEP*, 2022:083C01, 2022. doi:10.1093/ptep/ptac097. (pages 9, 44, 64).
- [16] T2K experiment. URL: <https://t2k-experiment.org/t2k/>. (pages 10, 61).
- [17] Aoi Eguchi. Development of Selection Algorithms for Electron Neutrino Interaction Events with New T2K Near Detectors ,Master’s thesis, Department of Physics, Graduate School of Science The University of Tokyo, 2021. (pages 12, 29, 32, 33, 40, 41, 42, 43, 61, 62, 64).
- [18] K. Abe et al.(T2K Collaboration). The T2K experiment. *Nuclear Instruments and Methods in Physics Research Section A*, 659, 12 2011. arXiv:<https://www.sciencedirect.com/science/article/pii/S0168900211011910/pdf?md5=d208854334ae30953097fec69690b872&pid=1-s2.0-S0168900211011910-main.pdf>, doi:10.1016/j.nima.2011.06.067. (pages 12, 15, 16, 17, 61).
- [19] K. Abe et al.(T2K Collaboration). Evidence of electron neutrino appearance in a muon neutrino beam. *Physical review D*, 88, 8 2013. doi:10.1103/PhysRevD.88.032002. (pages 14, 61).
- [20] P.A. Amaudruz et al. The T2K Fine-Grained Detectors. *Nuclear Instruments and Methods in Physics Research Section A*, 696, 12 2012. doi:10.1016/j.nima.2012.08.020. (page 14).

- [21] Dana Douqa on behalf of the T2K ND280 Upgrade group. The SuperFGD for the T2K near detector upgrade. *Journal of Physics: Conference Series*, 1690, 2020. URL: <https://iopscience.iop.org/article/10.1088/1742-6596/1690/1/012070>, arXiv:<https://iopscience.iop.org/article/10.1088/1742-6596/1690/1/012070/pdf>, doi:10.1088/1742-6596/1690/1/012070. (pages 15, 61).
- [22] N. Abgrall et al. Time projection chambers for the T2K near detectors. *Nuclear Instruments and Methods in Physics Research Section A*, 637, 5 2011. doi:10.1016/j.nima.2011.02.036. (pages 14, 35).
- [23] J-PARC press release. URL: <https://j-parc.jp/ja/topics/2016/Press160808.html>. (pages 16, 61).
- [24] K. Abe et al.(T2K Collaboration). Measurements of neutrino oscillation parameters from the T2K experiment using $3.6E21$ protons on target. *The European Physical Journal C*, 782, 9 2023. doi:10.1140/epjc/s10052-023-11819-x. (pages 17, 18, 19, 61).
- [25] K. Abe et al.(T2K Collaboration). Constraint on the matter-antimatter symmetry-violating phase in neutrino oscillations. *Nature*, 580, 6 2020. doi:10.1038/s41586-020-2177-0. (pages 17, 18, 64).
- [26] D. Barrow et al. T2K-SK joint nu oscillation sensitivity. *PoS*, NOW2022:008, 2023. doi:10.22323/1.421.0008. (page 19).
- [27] K. Abe et al. T2K ND280 Upgrade - Technical Design Report. 1 2019. arXiv: <https://doi.org/10.48550/arXiv.1901.03750>. (pages 23, 25, 26, 61, 62).
- [28] KURARAY Co. Wave length shifting fibers. URL: <http://kuraraypsf.jp/psf/ws.html>. (page 23).
- [29] Hamamatsu Photonics K.K. Multi-pixel photon counter. URL: https://www.hamamatsu.com/content/dam/hamamatsu-photonics/sites/documents/99_SALES_LIBRARY/ssd/s13360_series_kapd1052e.pdf. (page 24).
- [30] OMEGA-Centre de microélectronique Organisation de Micro Electronique Générale Avancée. CITIROC modules. URL: <https://portail.polytechnique.edu/omega/en>. (page 24).
- [31] T. Arihara et al. Development of the in-situ calibration system using leds and light guide plates for the superfgd. *J. Phys. Conf. Ser.*, 2374(1):012118, 2022. doi: 10.1088/1742-6596/2374/1/012118. (pages 24, 61).
- [32] Davide Sgalaberna. The T2K ND280 upgrade. *Proceedings of Science*, ICHEP2020:175, 2021. URL: <https://doi.org/10.3929/ethz-b-000484720>, doi: 10.22323/1.390.0175. (pages 26, 62).
- [33] iPad, Apple inc. URL: <https://www.apple.com/jp/ipad/>. (pages 28, 62).

- [34] Yoshinari Hayato and Luke Pickering. The NEUT neutrino interaction simulation program library. *The European Physical Journal Special Topics*, 230, 10 2021. doi: [10.1140/epjs/s11734-021-00287-7](https://doi.org/10.1140/epjs/s11734-021-00287-7). (page 30).
- [35] Geant4 overview. URL: <https://geant4.web.cern.ch/about/>. (page 31).
- [36] A.Blondel et al. The superfgd prototype charged particle beam tests. *JINST*, 15(12):P12003, 2020. arXiv:2008.08861, doi:10.1088/1748-0221/15/12/P12003. (page 31).
- [37] M. Daszykowski and B. Walczak. 2.29 - density-based clustering methods. In Steven D. Brown, Romá Tauler, and Beata Walczak, editors, *Comprehensive Chemometrics*, pages 635–654. Elsevier, Oxford, 2009. URL: <https://www.sciencedirect.com/science/article/pii/B9780444527011000673>, doi:10.1016/B978-044452701-1.00067-3. (page 33).
- [38] R. C. Prim. Shortest connection networks and some generalizations. *The Bell System Technical Journal*, 36(6):1389–1401, 1957. doi:10.1002/j.1538-7305.1957.tb01515.x. (page 33).
- [39] Machine learning with ROOT. URL: <https://root.cern/manual/tmva/>. (page 34).
- [40] Xingyu Zhao. Particle identification and momentum reconstruction in t2k superfgd detector, 6 2022. doi:10.5281/zenodo.6767579. (pages 34, 35, 62).
- [41] Aoi Eguchi. EM shower reconstruction and electron neutrino selection with the T2K SuperFGD detector., 6 2022. doi:10.5281/zenodo.6768535. (pages 43, 46, 63).